

Computational hemodynamic non-newtonian fluid-structure interaction simulation in a curved stenotic artery

Sireetorn Kuharat^{1*} , M. A. Chaudhry¹ , O. Anwar Bég¹ , Tasveer A. Bég² 

¹ Salford University, Dept. Mechanical/Aeronautical Engineering, MPESG, Corrosion Lab, 3-08, SEE Building, M54WT, England, United Kingdom

² Engineering Mechanics Research, Israfil House, Dickenson Rd., Manchester, M13, England, United Kingdom.

Abstract: This paper focuses on deploying Computational Fluid Dynamics (CFD) and Fluid-Structure Interaction (FSI) to investigate key characteristics associated with Cardiovascular Diseases (CVDs), a leading cause of global mortality. CVDs encompass various heart and blood vessel disorders, including coronary artery disease, stroke and atherosclerosis, which significantly impact arteries. Risk factors such as high blood pressure and obesity contribute to atherosclerosis, which is characterized by narrowed arteries due to fatty deposits, impeding blood flow and increasing heart attack and stroke risks. To simulate blood flow behaviour and its effects on artery stenosis formation, ANSYS-based CFD and monolithic (one-way) FSI analyses are deployed in this work. Extensive visualization of blood flow patterns relevant to patient-specific conditions is included using the non-Newtonian (Carreau shear-thinning) bio-rheological model. These simulations start with creating a three-dimensional patient artery model, followed by applying CFD/FSI methodologies to solve the equations iteratively with realistic boundary conditions. Velocity, pressure, wall shear stress (WSS), Von Mises stress and strain characteristics are all computed for multiple curvature cases and different stenotic depths. Factors such as blood viscosity, density and its non-Newtonian behaviour due to red blood cells are considered. FSI analysis extends CFD by including the interaction between blood flow and deformable (elastic) arterial walls, accounting for the arterial mechanical properties and the flow-induced pressure changes. Here we do not consider the two-way case where deformation in turn affects the flow, only the one-way case where the blood flow distorts the arterial wall. This approach allows for deeper insight into the interaction between rheological blood flow and elastic arterial walls which aids in highlighting high stress zones, recirculation and hemodynamic impedance of potential use in identifying rupture or plaque formation, contributing significantly to the management and prevention of CVDs. The novelties of the present study are the simultaneous consideration of rigorous visualization of hemodynamic characteristics for a wide range of stenotic depths of direct relevance to patient-specific conditions (both diastolic and systolic phases are included), inclusion of non-Newtonian (Carreau shear-thinning) bio-rheology, multiple arterial curvatures, and also flow-structural interaction analysis. Previous studies have invariably considered only aspects of these multiple features. This article therefore generalizes and significantly extends previous studies and will be of benefit to clinicians and other researchers engaged in computational medical fluid dynamics.

Key words: CFD; Monolithic FSI; hemodynamics; stenotic; non-Newtonian Carreau model.

1. Introduction

Cardiovascular diseases (CVDs) are a leading cause of global mortality. They include coronary artery disease, stroke, heart failure and peripheral artery disease, among many others. A key focus is on how these diseases affect arteries, which are vital for transporting oxy-

gen-rich blood throughout the body. Many risk factors contribute to CVDs, such as high blood pressure, high cholesterol, diabetes, obesity, ethnic background and lifestyle choices. A particularly prevalent cause of CVDs is atherosclerosis. Atherosclerosis is characterized by narrowed arteries due to fatty deposits, poses significant

*Corresponding author:

Email: S.Kuharat2@salford.ac.uk

Cite this article as:

Kuharat, S., Chaudhry, M. A., Bég, O.A., Bég, T. A. (2024). Computational hemodynamic non-newtonian fluid-structure interaction simulation in a curved stenotic artery. *European Mechanical Science*, 8(4): 226-256. <https://doi.org/10.26701/ems.1492905>

History dates:

Received: 31.05.2024, Revision Request: 25.06.2024, Last Revision Received: 25.09.2024, Accepted: 30.09.2024



© Author(s) 2024. This work is distributed under <https://creativecommons.org/licenses/by/4.0/>



risks for heart attack, stroke, and reduced oxygen supply to organs [1]. Fluid dynamic studies of blood flow have motivated significant attention in engineering sciences over the past 5 decades. An excellent perspective of hemodynamic modelling was provided by Goldsmith and Skalak [2] who reviewed both large and small arterial transport and identified many key aspects including Newtonian and non-Newtonian behaviour, pulsatile and pressure wave propagation, bifurcations, curvature, bends, obstructions and stenoses. They emphasized the importance of including curvature and rheological effects, in particular, in the microcirculation and the contribution to the genesis of atherosclerotic and other pathological states. More recently Ku [3] reviewed key progress in the two decades following the review of Goldsmith and Skalak [2], focusing on unsteady characteristics in cardiovascular flows, multiple branching, Womersley number, curvature and computational and diagnostic tools. Further excellent perspectives on hemodynamic simulation have been given by Taylor and Figueroa [4] addressing finite element and fluid-structure interaction for patient-specific geometries and Wong *et al.* [5] on coronary artery hemodynamics focusing on Computed Tomography (CT) imaging, WSS and wall pressure (WPG) and their contribution to atherosclerosis and plaque formation, which in turn leads to myocardial ischemia and infarction. A particularly important geometrical configuration in hemodynamics is a stenosis. Atherosclerotic disease is confirmed to be localized in zones where there is a narrowing of the artery lumen; this is known as a stenosis. The stenosis can induce significant modifications in velocity distribution, experiences impedance via viscous head losses and flow choking. Berger [6] has further identified that stenotic conditions are more prevalent in zones where the vessel is curved, exhibits a split (bifurcation), junction, side branch or rapid change in geometry. These flows may also feature flow reversal, separation, low and oscillating wall shear stresses, secondary vortices etc, which are very challenging to simulate. Substantially high shear stresses may arise in the vicinity of the throat of the stenosis which in turn can activate platelets and this can accelerate the onset of thrombosis manifesting in serious blockage to blood flow to the heart or brain. Stenotic hydrodynamics is therefore a very important aspect of blood flow modelling. Mathematical modelling of stenotic and/or curved arterial transport can therefore significantly benefit early detection and quantification of stenosis and advise clinicians in terms of surgical intervention, stenting or coronary bypass surgery. Many interesting studies in both these areas have been communicated in recent years. Dash *et al.* [7] investigated Newtonian blood flow in a catheterized curved artery with stenosis under steady and laminar conditions. They derived double series perturbation solutions for the case of small curvature and mild stenosis. They computed the effect of catheterization on pressure drop, impedance and the wall shear stress for a range of catheter size and Reynolds numbers, noting significant variation across the stenotic lesion and that elevation in catheter size enhances all flow charac-

teristics. They also demonstrated that the effect of stenosis is more dominant than that of the curvature. Kim *et al.* [8] deployed modified coronary angiography, to measure the functional significance of a stenosis, specifically pressure drop across the stenosis. They also simulated the regime with 3D finite element simulations for thirty-three patient-specific coronary stenoses. They identified that pressure drop is principally attributable to curvature as well as the area-reduction ratio of the stenosis before the minimal luminal area (MLA), although it is also influenced significantly by the area-expansion ratio after the MLA due to flow separation. Santamarina *et al.*, [9] investigated the hemodynamics in a curved tube model of the coronary artery with sinusoidally time-varying curvature using CFD-ACE software. They considered an inlet steady uniform velocity corresponding to a Reynolds number of 300 and observed a variation in wall shear rates in excess of 50% relative to the static mean wall shear rate within a region of 10 tube diameters from the inlet. to, flow patterns that have been associated with atherogenesis. Hoque *et al.* [10] investigated the biomagnetic blood flow in a curved tube arterial model with a spectral numerical method, as a simulation of ionic behaviour in streaming hemodynamics. They computed Dean vortex structures for a range of magnetic Hartmann numbers and also curvature ratios. Many other investigations have been communicated in curved conduit biological fluid dynamics. Chiang *et al.* [11] used a finite volume method (FVM) to simulate the viscous Newtonian unsteady blood flow and vortex patterns in a 180° curved arterial geometry. Ali *et al.* [12] who examined peristaltic blood flow in a curved conduit with the Carreau rheological model, forward time centre spaced (FTCS) finite difference and variational finite element methods. Tripathi *et al.* [13] deployed the Nakayama-Sawada bi-viscosity non-Newtonian model and MATLAB quadrature for curved tube biological transport. Narla *et al.* [14] considered axial electrical field effects on nano-doped blood flows in a curved microvascular geometry. Khan *et al.* [15] utilized integral and Mathematica shooting methods to compute the electrokinetic peristaltic pumping of ionic blood with viscous heating in a curved micro-channel. Bég *et al.* [16] visualized the Dean vortex patterns in curved arterial magnetized blood flow with numerical methods. Many complex stenotic hemodynamics simulations have also been reported recently using both Newtonian and non-Newtonian formulations. Non-Newtonian models better represent the complex properties of blood in smaller geometries which are associated with suspensions in including blood cells, proteins, lipids etc. These alter the rheology of streaming blood. Zaman *et al.* [17] computed the time-dependent magnetic pseudoplastic blood flow with body acceleration in an overlapping stenotic artery containing porous media (fatty deposits) with finite difference techniques. They showed that with higher values of permeability parameter, there is a boost in velocity, flow rate and wall shear stress increase and a concomitant reduction in hemodynamic impedance and also contraction in the magnitude of trapped boluses of blood. They further not-

ed that stronger transverse extra-corporeal magnetic field retards the blood flow, enhances impedance and modifies the post-stenotic flow distribution significantly. Wajihah and Sankar [18] reviewed a variety of stenotic hemodynamic models utilizing the single-layered viscoelastic rheological and also four-layered fluid models (combinations of Newtonian peripheral and core non-Newtonian power-law models). Sriyab *et al.* [19] computed the blood flow in power-law non-Newtonian blood flow through different stenoses, namely bell- and cosine shaped geometries. They noted that blood flow in the cosine geometry experiences greater impedance compared with the bell geometry, whereas the latter produces higher wall shear stress magnitudes. They also computed the influence of stenosis depth and stenosis height on flow characteristics over a range of values of the rheological power law index. Lakzian *et al.* [20] investigated the Newtonian/non-Newtonian unsteady pulsatile entry blood flow inside a 3D curved stenosed artery using the power-law model to characterize shear thinning or shear thickening behaviour. They applied a clinically robust pulsatile waveform at the inlet of the artery, and examined the impact of its curvature ratios, percentage and length ratio of stenosis and shear-thickening on hemodynamic characteristics, noting that the maximum wall shear stress arises in the vicinity of the stenosis (constriction) and that wall shear stress is elevated with a reduction in stenosis length. Zaman *et al.* [21] numerically studied the transient non-Newtonian blood flow through a diseased catheterized artery featuring both a stenosis and post-stenotic dilated region, using the Eringen micropolar model. They noted that blood velocity and flow rate are suppressed whereas hemodynamic impedance is enhanced with an increment in size of catheter radius, critical height parameter and micropolar parameter in the stenotic region, whereas the opposite behaviour is computed in the post-stenotic dilated region. They further visualized the post-stenotic vortex patterns and noted that the strength of recirculating zones appearing in this location is also an increasing function of catheter radius, critical height parameter and micropolar parameter. Further investigations of stenotic hemodynamics include Vasu *et al.* [22] (who deployed FreeFEM++ software and also considered nanoparticle drug diffusion), Tripathi *et al.* [23] (who considered magnetohydrodynamic control in nano-doped blood flow in an axisymmetric overlapped stenotic artery), Dubey *et al.* [24] (who utilized a Sisko viscoelastic model for Ag-Au nanoparticle blood transport in an irregular symmetric stenosis) and Roy and Bég [25] (who used asymptotic methods to study Taylor dispersion in time-dependent blood flow and mass diffusion in multiple irregular stenoses). Other computational models of stenotic blood flows have deployed the Cross rheological model [27], Oldroyd-b viscoelastic model [28], Reynolds exponential viscosity model [29] and Sisko viscoelastic and Buongiorno nanoscale models [30].

The above studies, while they have all confirmed the significant modification in hemodynamic characteristics

with rheology, have neglected deformability of the blood vessel. When the blood flow distorts the vessel geometry and this geometry then alters the blood flow, this two-way coupling is known as fluid structure interaction (FSI). It is very prominent in the cardiovascular system as exemplified by the beating of the human heart, expansion and contraction of arterial and venous segments. It also arises in human respiration, intestinal peristalsis etc. To more accurately represent actual hemodynamic transport therefore, FSI models are required. Understandably the simulation of blood flow/vessel structural interaction is computationally much more challenging than purely hemodynamic modelling. Recent advances in algorithms available in commercial computational fluid dynamics (CFD) software and hardware however have enabled FSI computations to be conducted in reasonable compilation times and with much improved accuracy. FSI enables simultaneously the computation of both fluid dynamic characteristics (pressure, velocity, vorticity, wall shear stress) and also structural characteristics (deformation, stress and strain). Many excellent studies have therefore been communicated in the past decade. Bukač *et al.* [31] used a loosely coupled partitioned finite element method to compute the FSI between a curved (tortuous) coronary artery with an implanted stent, pulsatile Newtonian blood flow, and heart contractions. They considered a variety of stent geometries (Palmaz-like stent, an Express-like stent, Cypher-like stent and a Xience-like stent) and simulated the arterial walls as multi-layered different structures (the intimal layer with the internal elastic laminae as a nonlinearly elastic membrane and the media-adventitia complex as a 3D linearly elastic material). Bukač *et al.* [32] further investigated hemodynamic FSI problems with a coupled partitioned numerical scheme allowing non-zero longitudinal displacement in which arterial walls were simulated as linearly viscoelastic, cylindrical Koiter shells and a Newtonian viscous model was deployed for blood. Mendez *et al.* [33] studied 2-way FSI in blood flow in ascending thoracic aortic aneurysms (ATAAs) with both a bicuspid aortic valve (BAV) and separately with a tricuspid aortic valve (TAV). Carvalho *et al.* [34], motivated by elaborating more precisely the artery wall interaction with streaming blood, utilized both computational fluid dynamics and fluid-structure interaction modelling analysis to investigate if the arterial wall compliance affect considerably the hemodynamic results obtained in idealized stenotic coronary models. They confirmed that the impact of wall compliance on wall shear stress distribution is significantly greater than on the time-averaged wall shear stress and on the oscillatory shear index. This study is also notable for emphasizing the importance of mesh quality for accurate simulations and utilized a 50% stenosis model without curvature, which limits the understanding of wall shear effects but provides valuable insights into fluid properties and modelling. Luraghi *et al.* [35] deployed HYPERMESH, ANSYS and LS-DYNA finite element codes to compute the FSI in blood flow in bio-inspired polymeric heart valves (PHVs). They noted that, FSI simulations are substantially more accurate

than purely CFD or Finite element stress simulations to describe the actual behaviour of PHVs as they can replicate the valve-fluid interaction while providing realistic fluid dynamic results. Failer *et al.* [37] conducted monolithic (one way) FSI simulations of Newtonian blood flow in curved elastic arteries. They evaluated the impact of FSI on the wall shear stress distribution, fractional flow reserve and on the damping effect of a stenosis on the pressure amplitude during the pulsatile cycle. Further investigations of stenotic FSI blood flows include Balzani *et al.* [37] (who deployed both different nonlinear wall models to better simulate vascular elasticity including anisotropic and simple, isotropic Neo-Hooke models), Deparis *et al.* [38] (who used Steklov–Poincaré Formulation for FSI coupling in blood flow in compliant arteries), Gasser *et al.* [39] (who considered FSI simulations in biomechanical rupture risk assessment of abdominal aortic aneurysms), Turek *et al.* [40] (who utilized monolithic multigrid finite element codes) and Bertaglia *et al.* [41] (who employed viscoelastic wall models).

Motivated by exploring in more detail fully 3D stenotic and curved arterial geometry hemodynamics with wall compliance, in this article CFD and FSI approaches are utilized to investigate key characteristics of blood flow behaviour and its effects on artery stenosis formation. ANSYS-based CFD and FSI analyses are deployed in this work. Extensive visualization of blood flow patterns relevant to patient-specific conditions is included using both the non-Newtonian (Carreau shear-thinning) bio-rheological model. Velocity, pressure, wall shear stress (WSS), stress and strain characteristics are all computed for multiple curvature cases and different stenotic depths. These simulations start with creating a three-dimensional patient-specific artery model, followed by applying CFD and FSI methodologies to solve the equations iteratively with realistic boundary conditions. FSI analysis extends CFD by including the interaction between blood flow and deformable (elastic) arterial walls, accounting for the arterial mechanical properties and the flow-induced pressure changes. Detailed contour plots are presented with extensive interpretation of the results and clinical implications for cardiovascular disease. The present study has identified that thus far there has been an absence in computational hemodynamics literature with regard to the *simultaneous consideration of rigorous visualization of hemodynamic characteristics for a wide range of stenotic depths of direct relevance to patient-specific conditions (both diastolic and systolic phases are included), inclusion of non-Newtonian (Carreau shear-thinning) bio-rheology, multiple arterial curvatures, and also flow-structural interaction analysis.* These are all addressed for the first time in the present article which generalizes and pushes forward on previous studies which were restricted to only aspects of these multiple features and did not consider all these features. This article therefore generalizes and significantly extends previous studies and will be of benefit to clinicians and other researchers engaged in computational medical fluid dynamics.

2. Methodolog

2.1. Fluid Dynamic Models and Wall shear stress

The basic viscous flow model available in ANSYS FLUENT is Newtonian for which we adopt the incompressible Navier–Stokes and the continuity equations as shown below:

$$\nabla \cdot \mathbf{u} = 0 \quad (1)$$

$$\mu_0 = 0.0560 Pa \cdot s \quad (2)$$

Here, \mathbf{u} is the velocity vector, ρ is density, t is time, p is pressure and μ is dynamic viscosity. The flow is modelled as incompressible and laminar with a density of 1060 kg/m^3 following McDonald [42]. However, due to the capacity of red blood cells to deform and aggregate, blood is actually a non-Newtonian fluid. In this work, we therefore adopt the *non-Newtonian Carreau* model which accurately represents the shear-thinning blood behaviour, and is defined by equation below:

$$\mu = \mu_\infty + (\mu_0 - \mu_\infty) [1 + \lambda \dot{\gamma}^2]^{\frac{n-1}{2}} \quad (3)$$

Here the μ is viscosity, $\mu_\infty = 0.00345 Pa \cdot s$ is the infinite shear viscosity, $\mu_0 = 0.0560 Pa \cdot s$ is the blood viscosity at zero shear rate, $\lambda = 3.13s$ is the time constant, $\dot{\gamma}$ is the instantaneous shear rate and $n = 0.3568$ is the rheological power-law index. Selection of the Carreau model option in ANSYS FLUENT modifies the appropriate terms in the basic Newtonian viscous model. Many applications of this model have been communicated in previous studies in blood flows [43–50]. A key hemodynamic parameter is the WSS which is useful for predicting and estimating distributed flow conditions and the development of local atherosclerotic plaque. WSS is calculated using:

$$\tau_w = \mu \frac{\partial u}{\partial y} = \mu \cdot \dot{\gamma} \quad (4)$$

Here $\dot{\gamma}$ is deformation rate and $\frac{\partial u}{\partial y}$ is axial spatial velocity gradient.

2.2. Boundary Conditions

In terms of the boundary conditions applied in this investigation, a medically precise pulsatile velocity profile was set at the inlet and is shown in ►Figure 1 and 80 mmHg of pressure was predicated for the outflow based on the study done by Carvalho *et al.* [34]. The inlet and outlet are fixed in all directions, and the vessel wall boundaries are established as a fluid-structure interface. The pulsative velocity profile is converted into a text file and inserted into the analysis as shown in the ►Figure 1.

The elastic artery wall material has a density of $\rho = 1120 \text{ kg/m}^3$. The ANSYS Fluent software applies the finite discretisation method to divide the fluid domain into finite control volumes and apply conservation equations to each volume. The semi-implicit approach for the pressure-linked equations (SIMPLE) methodology is employed for the velocity-pressure coupling [34]. The CFD simulation is set as transient due to the heartbeat and pulsation effect. The results for CFD analysis include velocity plots, wall shear stress and pressure at the peak points of systole (0.4) and diastole (0.6). These points are chosen due to the extreme conditions applied to the system.

2.3. Hemodynamic Geometry

In the present simulations, we study various degrees of curvature of the arteries and different percentages of stenosis. Properties of the artery are taken from [34]. The maximum thickness of this artery is considered to be 0.8mm. The solid geometry is used in CFD, and the shell geometry is used in the FSI analysis. The fluid domain is created using design modular in Ansys workbench [51]. The straight length of the artery is estimated to be 20mm long and the diameter is 2.9mm based on the study [42]. Three different curvatures are given to the geometry with the angles of 30°, 60° and 90°. The percentage of stenosis severity is illustrated in ►Figures 2-4 for each angle. The blood flow travels from the bottom of the curved artery to the top.

2.4. Meshing

After creating the geometry, it is discretised using a mesh tool before boundary conditions can be applied. The element size of 0.11mm is used to discretize the fluid domain into hexahedral elements. The artery due its cylindrical shape will require an inflation feature closer to the wall which allows elements to be smaller in the

near wall region. This is done to capture more precisely the wall velocity profile and wall shear stress. Five inflation layers are applied near to the wall area with a growth rate of 1.2 transitioning smoothly along the wall. The meshes are visualized in ►Figure 5.

The smallest possible element size of 0.11mm is used to generate mesh. To ensure the quality of the mesh, the skewness and orthogonal quality are evaluated. The maximum skewness and minimum Orthogonal quality parameters as documented in ►Table 1 below show that the mesh quality is reliable, and convergence is achieved.

3. Numerical CFD And FSI Contour Results Visualization

Detailed simulations have been conducted. The sim-

Table 1. Mesh independence tests conducted with skewness

Curvature (degree)	% Stenosis	No of Element	Min Orthogonal Quality	Max Skewness
30	20	441688	0.338	0.662
60	20	427180	0.335	0.665
90	20	366639	0.56	0.44
30	40	441688	0.338	0.662
60	40	427180	0.335	0.665
90	40	366639	0.557	0.443
30	60	441688	0.338	0.662
60	60	427180	0.336	0.664
90	60	366639	0.55	0.451
30	80	444912	0.338	0.662
60	80	430404	0.337	0.663
90	80	369733	0.506	0.502

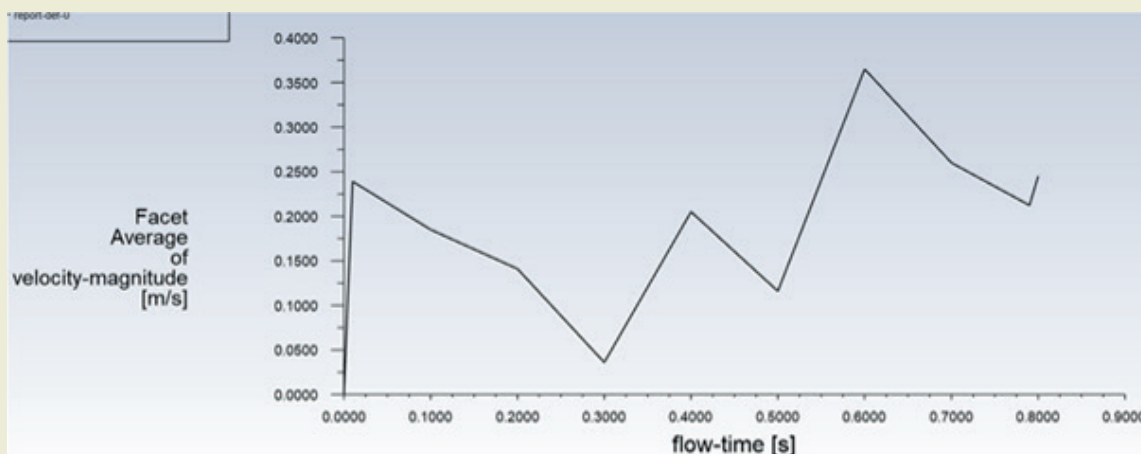


Figure 1. Pulsatile wave form deployed in simulations.

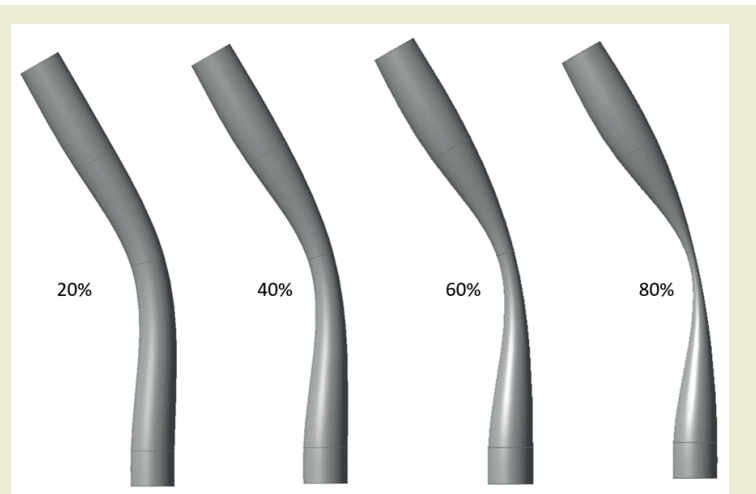


Figure 2. 30-degree curved arteries with different percentage of stenosis

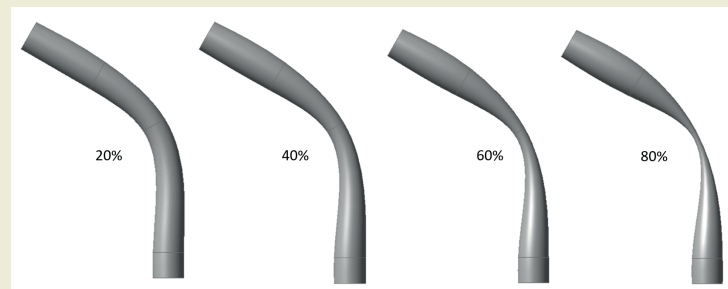


Figure 3. 60-degree curved arteries with different percentage of stenosis.

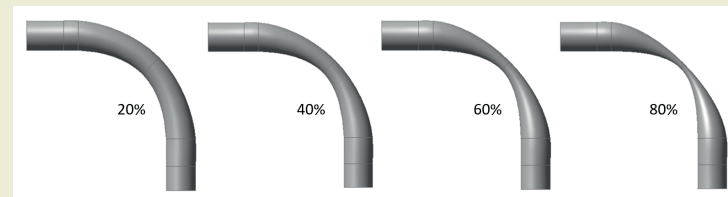


Figure 4. 90-degree curved arteries with different percentage of stenosis.

ulations have been grouped according to curvature with corresponding variations in stenosis percentage for each case of curvature. It is important again to mention that only one-way coupling is considered in the FSI simulations, wherein the blood flow distorts the arterial walls; the arterial walls do not modify the blood flow. This was selected as a first step in order to establish a rigorous methodology for cardiovascular FSI. In subsequent studies the authors will examine the full two-way coupling problem and also explore other non-Newtonian models e.g. power-law model, Casson viscoplastic model etc, which are also available in the ANSYS workbench platform.

3.1. CFD Visualizations

We present first the CFD results for velocity (streamlines), pressure, wall shear stress and finally 3D velocity vector plots for 3 curvature cases (30, 60, 90 degrees) each with 4 stenosis depths (20, 40, 60, 80%). The results are therefore grouped in 12 sets in 4 subsections (A, B, C, D). In each figure we provide 2 graphs, one for the *systole* (the part of the cardiac cycle during which some chambers of the heart contract after refilling with blood) and the other for the *diastole* (relaxed phase of the cardiac cycle when the chambers of the heart are refilling with blood. The contrasting phase is systole when the heart chambers are contracting).

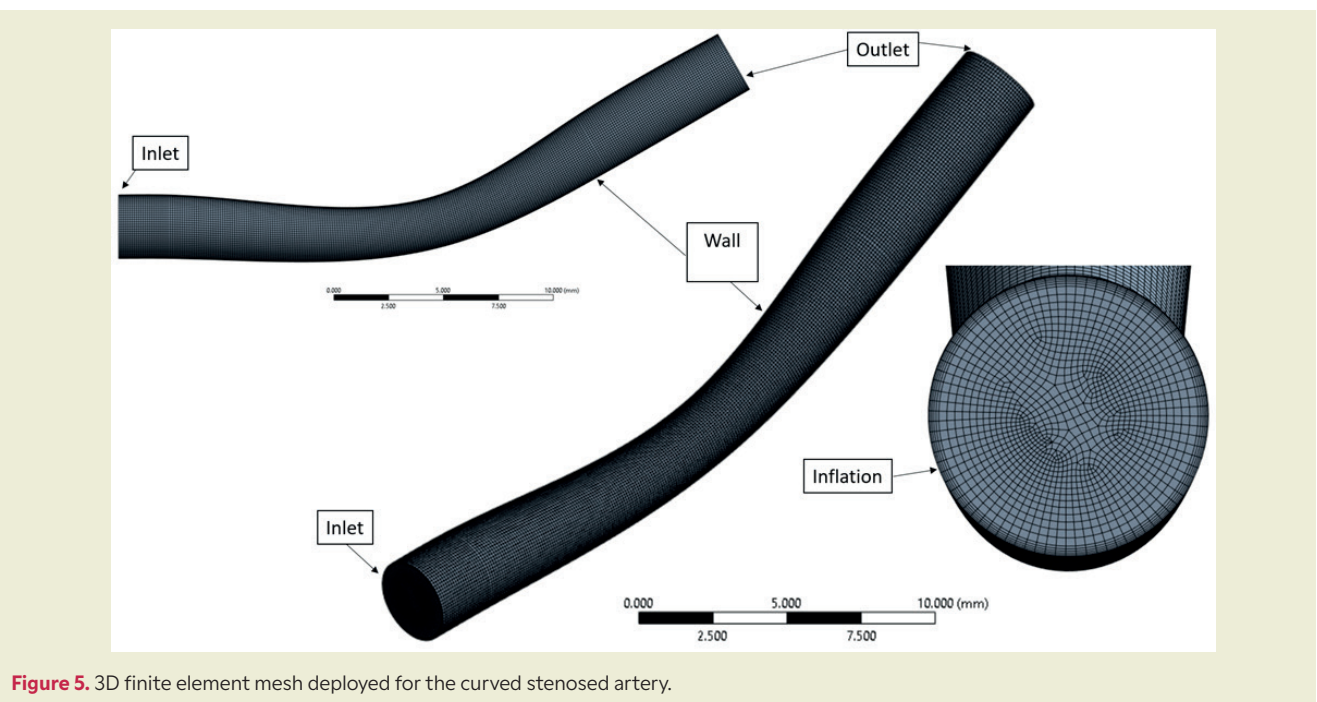


Figure 5. 3D finite element mesh deployed for the curved stenosed artery.

3.1-1 Velocity contours for different curvatures and stenoses

A) Velocity contour of 30-degree curvature

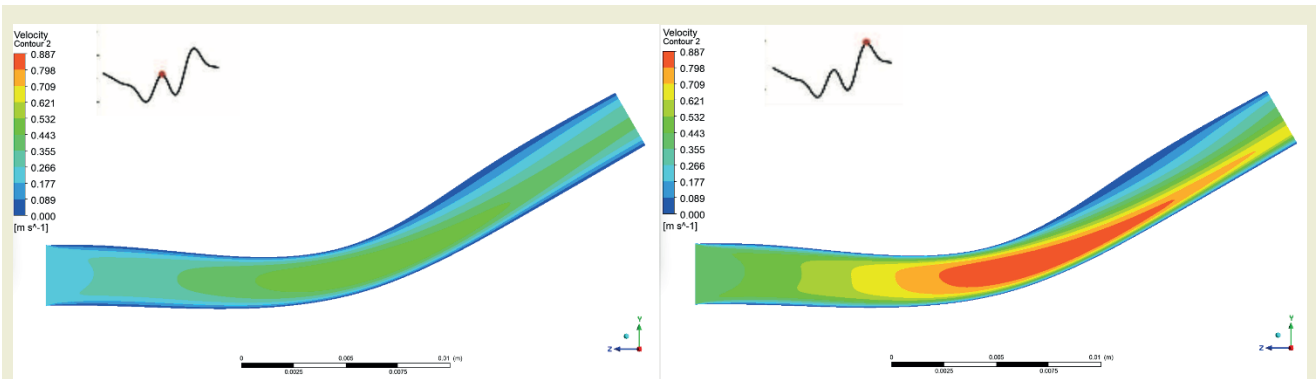


Figure 6. Velocity contour of systole (left) and diastole (right) with 20% stenosis.

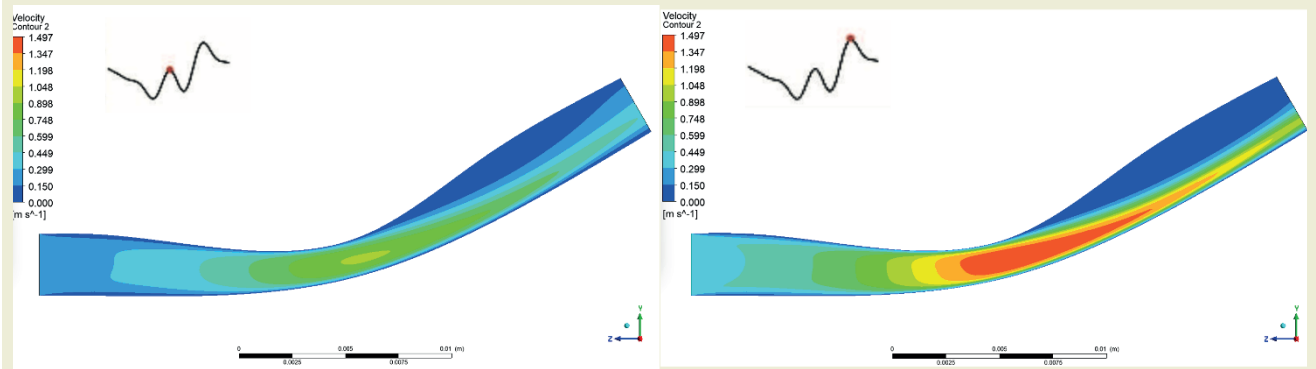


Figure 7. Velocity contour of systole (left) and diastole (right) with 40% stenosis.

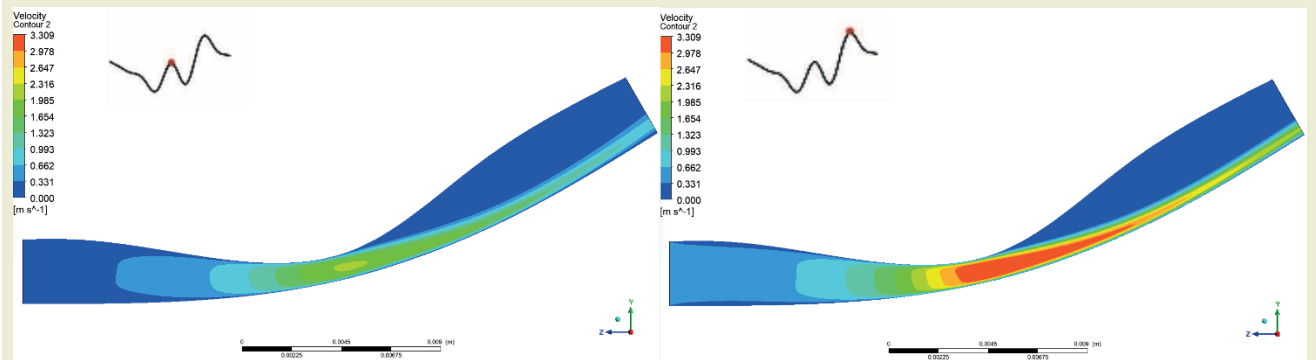


Figure 8. Velocity contour of systole (left) and diastole (right) with 60% stenosis.

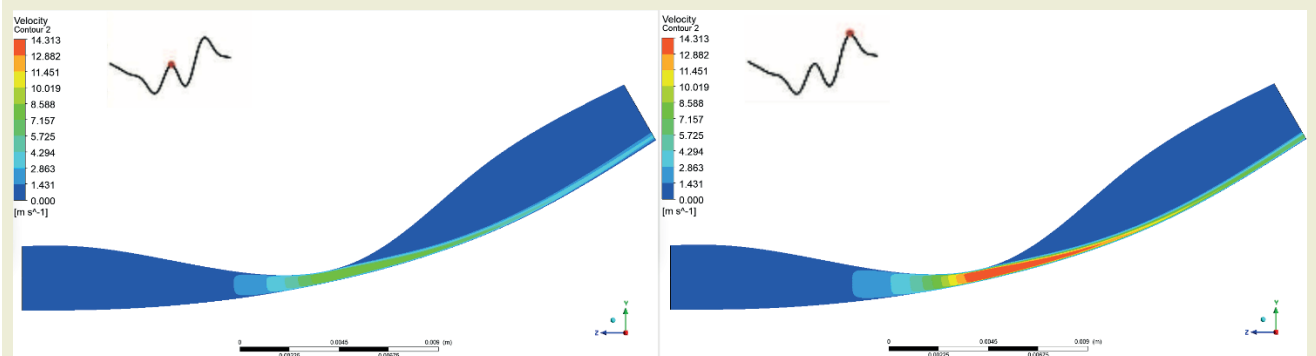


Figure 9. Velocity contour of systole (left) and diastole (right) with 80% stenosis.

B] Velocity contour of 60-degree curvature

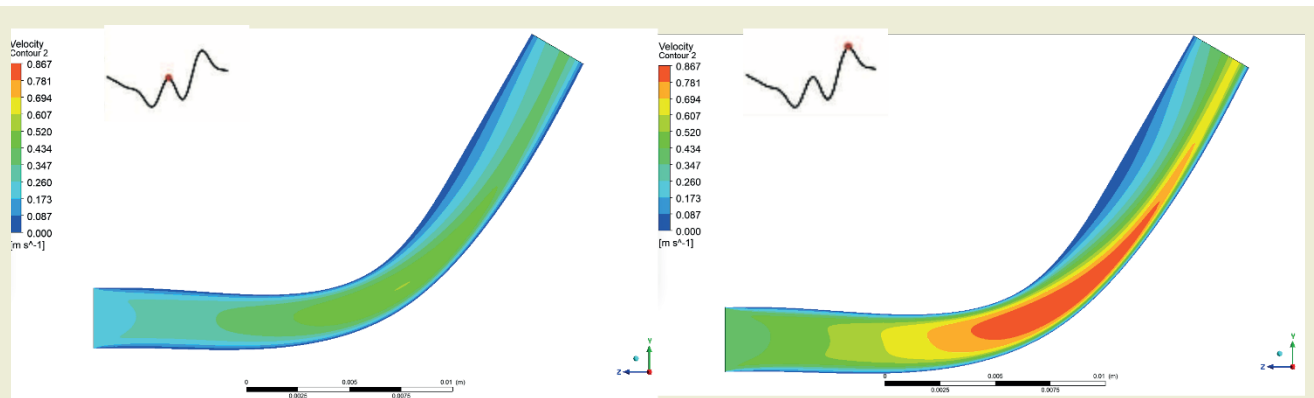


Figure 10. Velocity contour of systole (left) and diastole (right) with 20% stenosis.

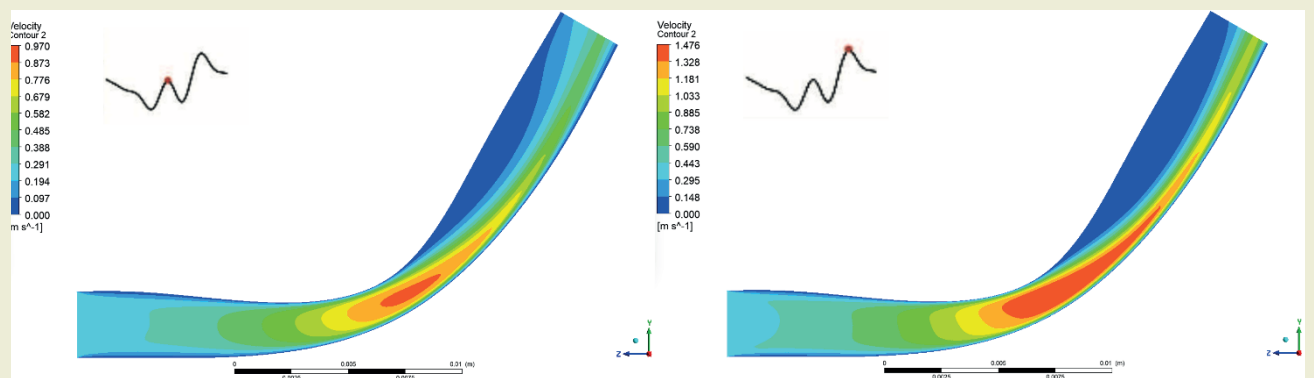


Figure 11. Velocity contour of systole (left) and diastole (right) with 40% stenosis.

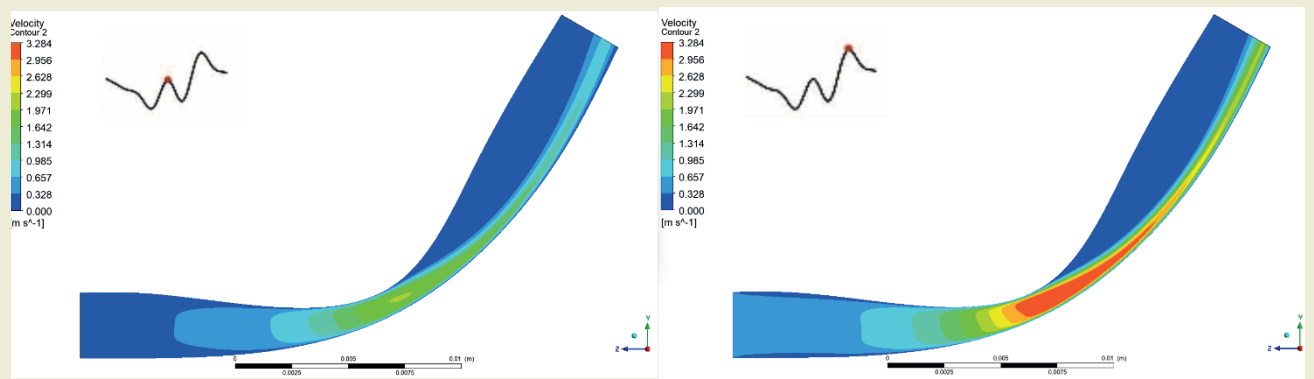


Figure 12. Velocity contour of systole (left) and diastole (right) with 60% stenosis.

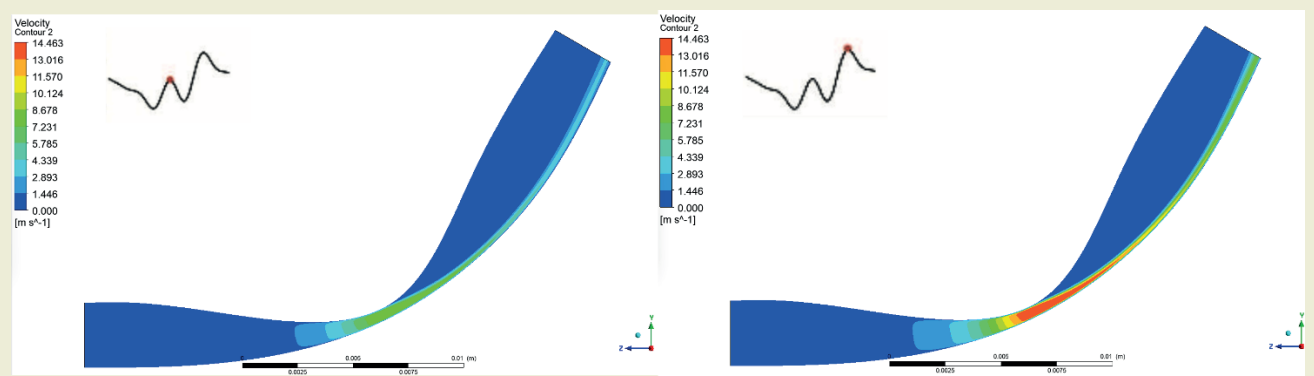


Figure 13. Velocity contour of systole (left) and diastole (right) with 80% stenosis.

C] Velocity contour of 90-degree curvature

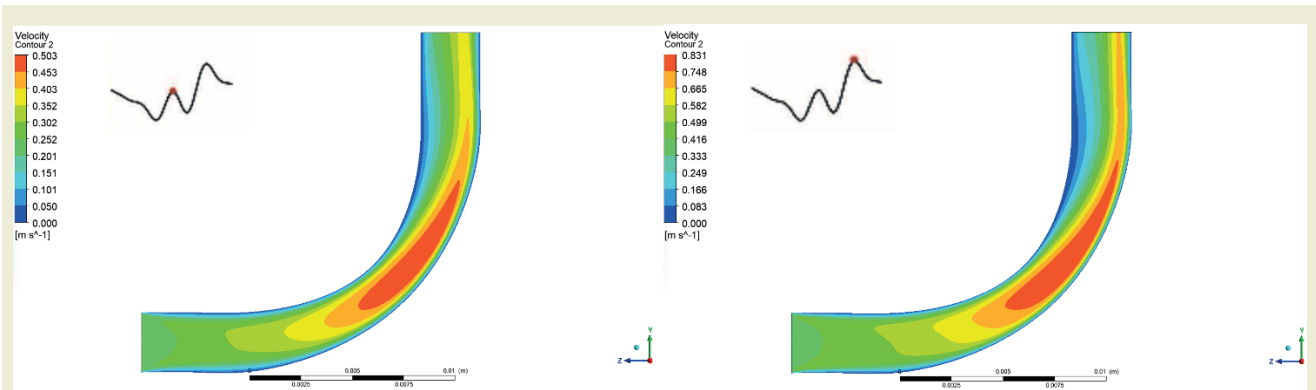


Figure 14. Velocity contour of systole (left) and diastole (right) with 20% stenosis.

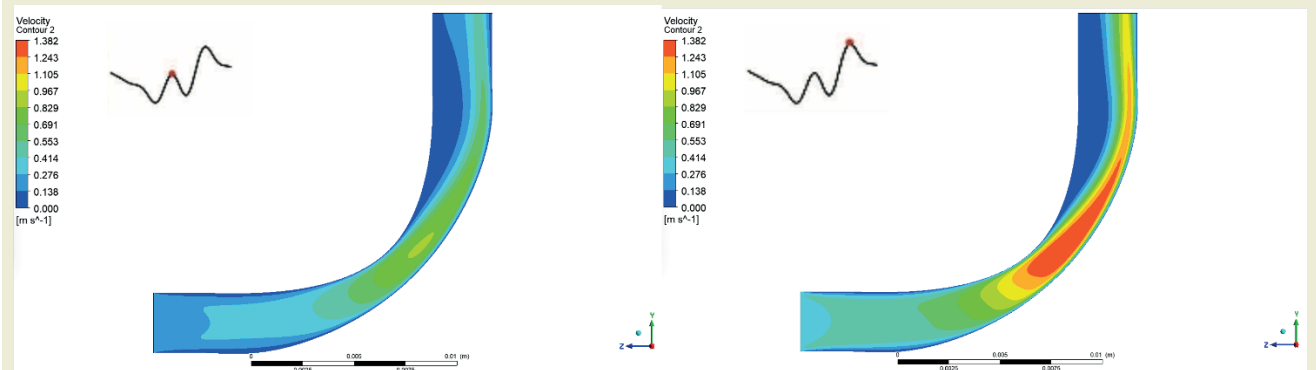


Figure 15. Velocity contour of systole (left) and diastole (right) with 40% stenosis.

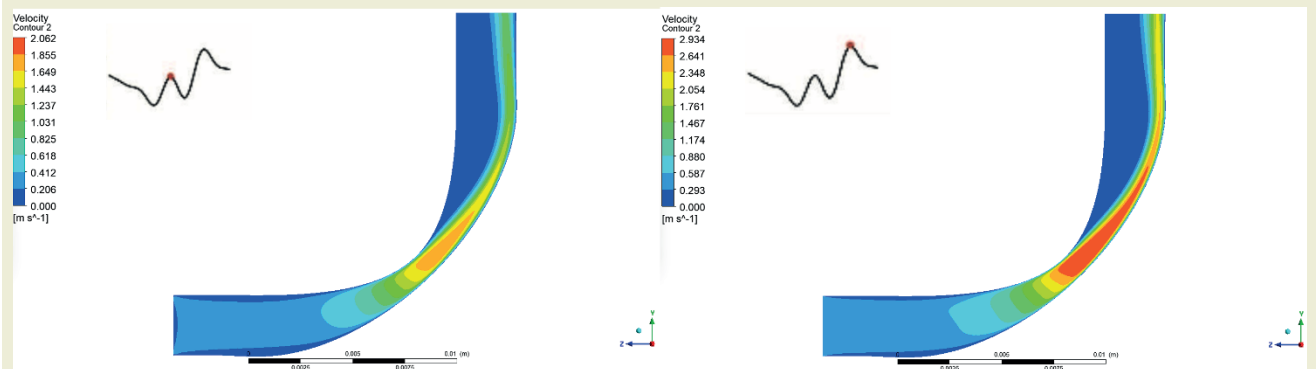


Figure 16. Velocity contour of systole (left) and diastole (right) with 60% stenosis.

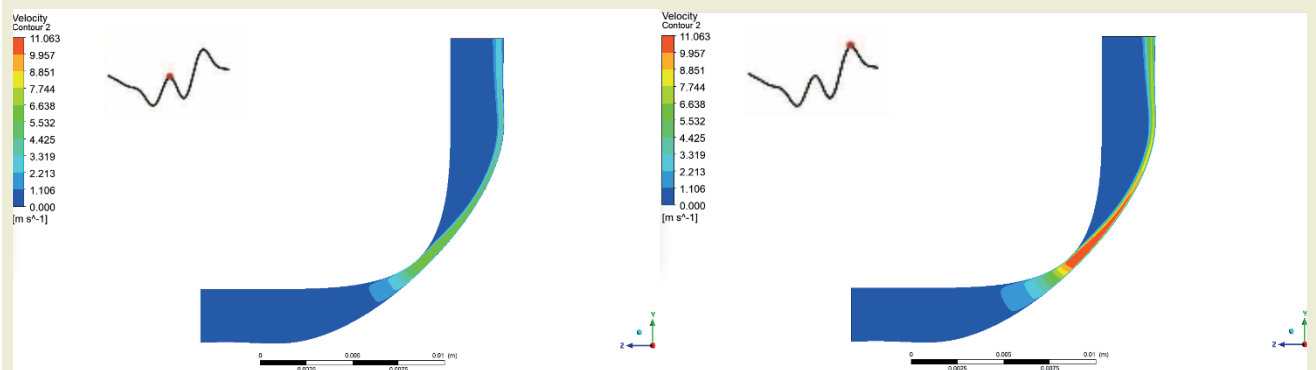


Figure 17. Velocity contour of systole (left) and diastole (right) with 80% stenosis.

3.1-2 Pressure contours for different curvatures and stenoses

A] Pressure contour of 30-degree curvature

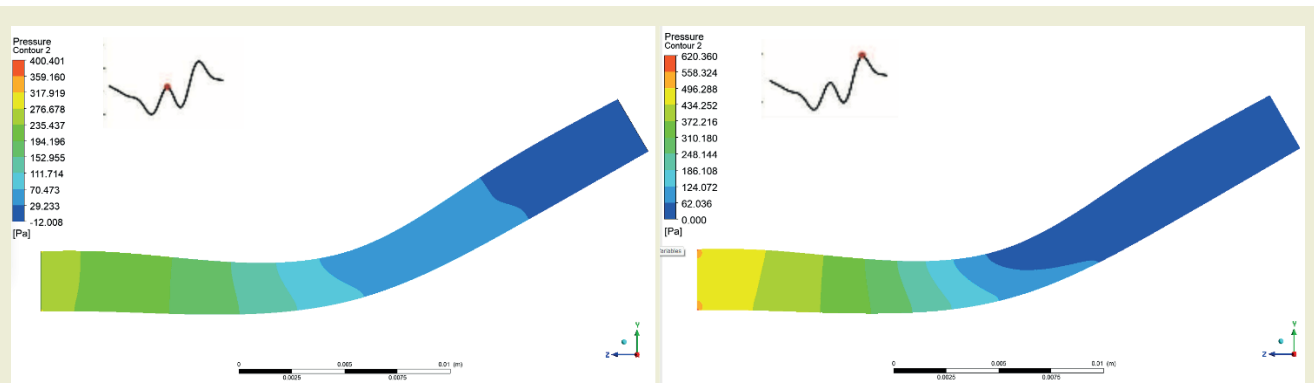


Figure 18. Pressure contour of systole (left) and diastole (right) with 20% stenosis.

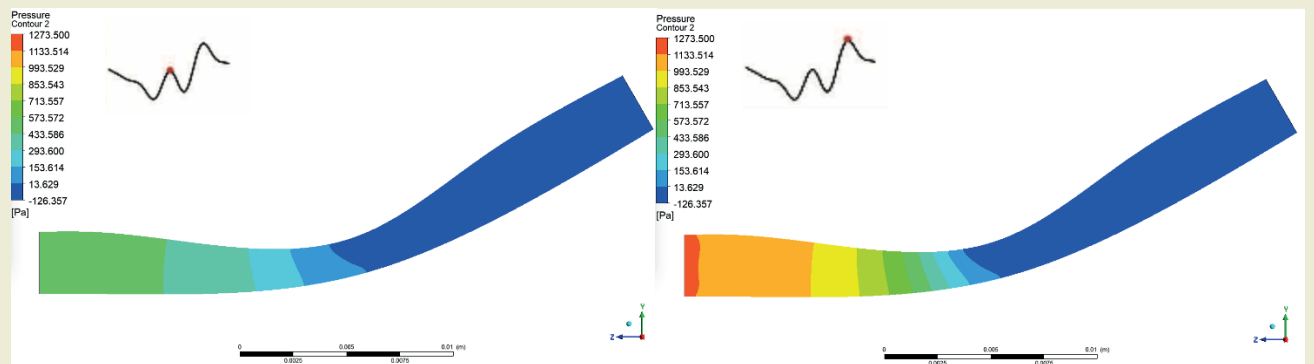


Figure 19. Pressure contour of systole (left) and diastole (right) with 40% stenosis.

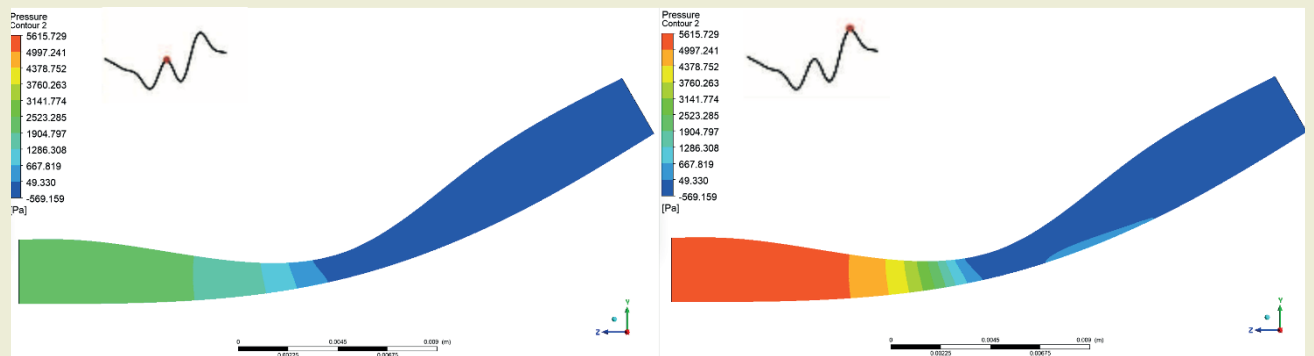


Figure 20. Pressure contour of systole (left) and diastole (right) with 60% stenosis.

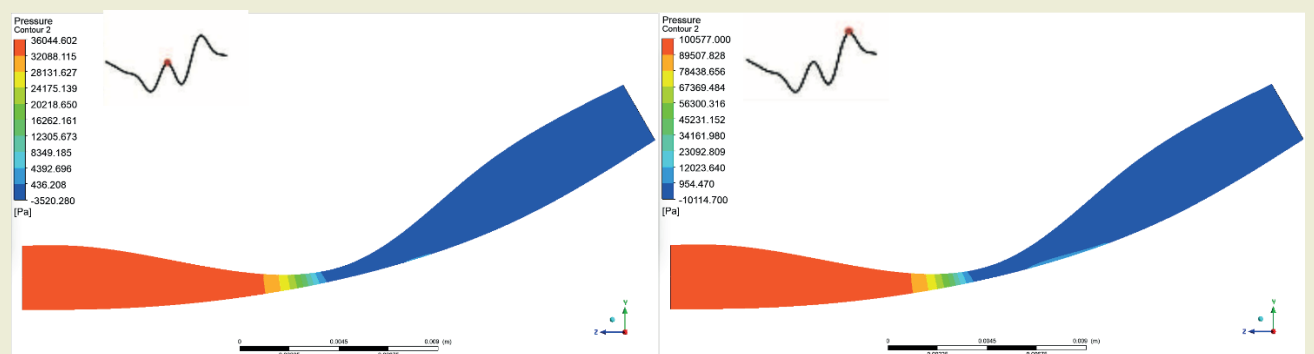


Figure 21. Pressure contour of systole (left) and diastole (right) with 80% stenosis.

B) Pressure contour of 60-degree curvature

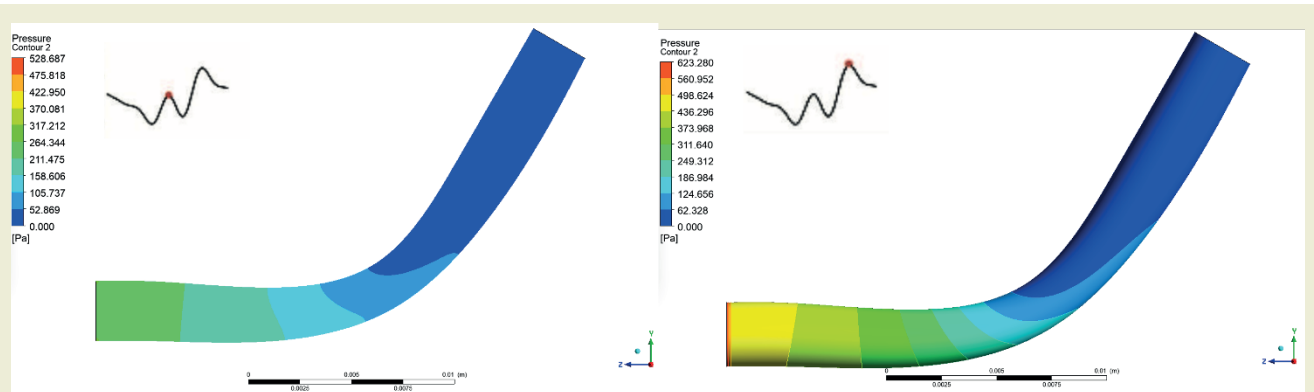


Figure 22. Pressure contour of systole (left) and diastole (right) with 20% stenosis.

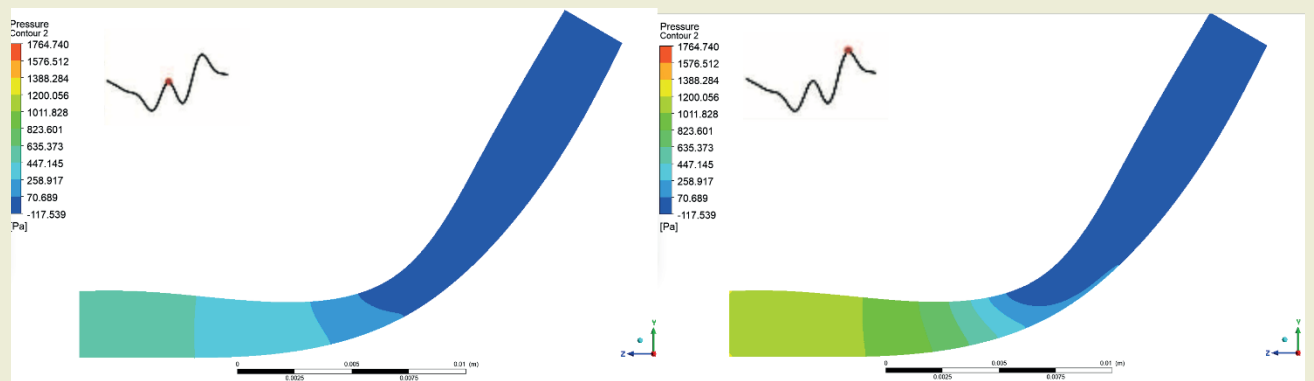


Figure 23. Pressure contour of systole (left) and diastole (right) with 40% stenosis.

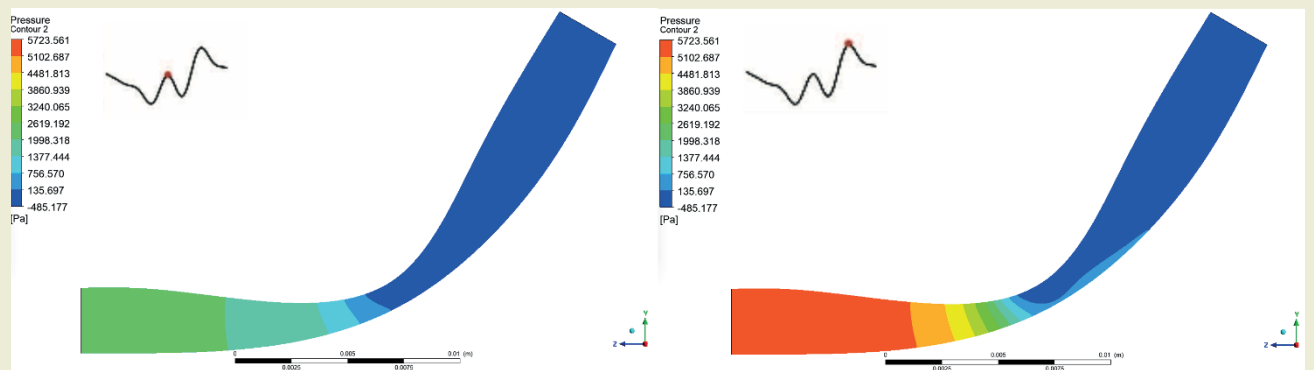


Figure 24. Pressure contour of systole (left) and diastole (right) with 60% stenosis.

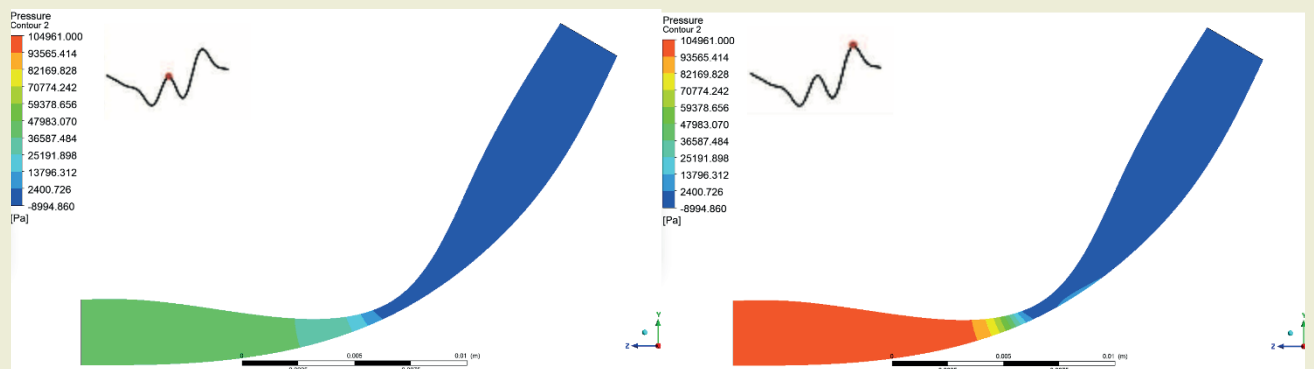


Figure 25. Pressure contour of systole (left) and diastole (right) with 80% stenosis.

C] Pressure contour of 90-degree curvature

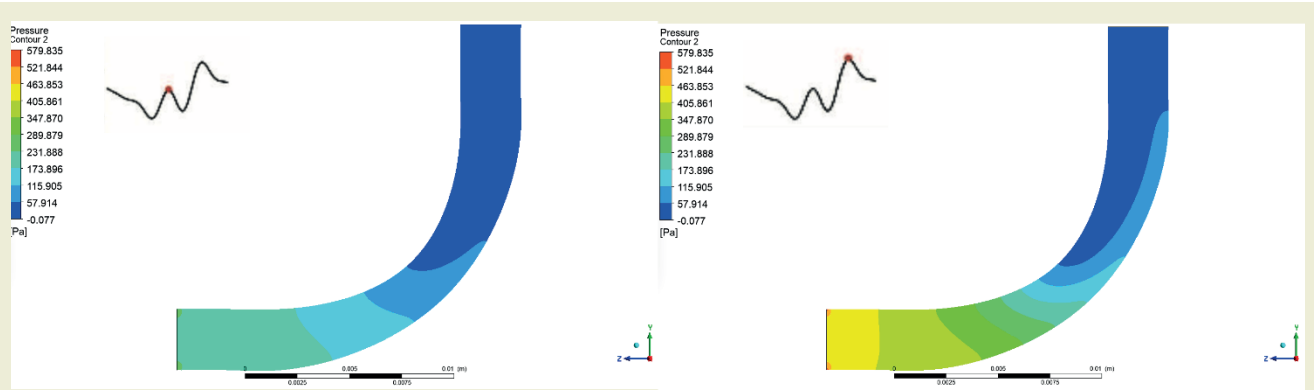


Figure 26. Pressure contour of systole (left) and diastole (right) with 20% stenosis.

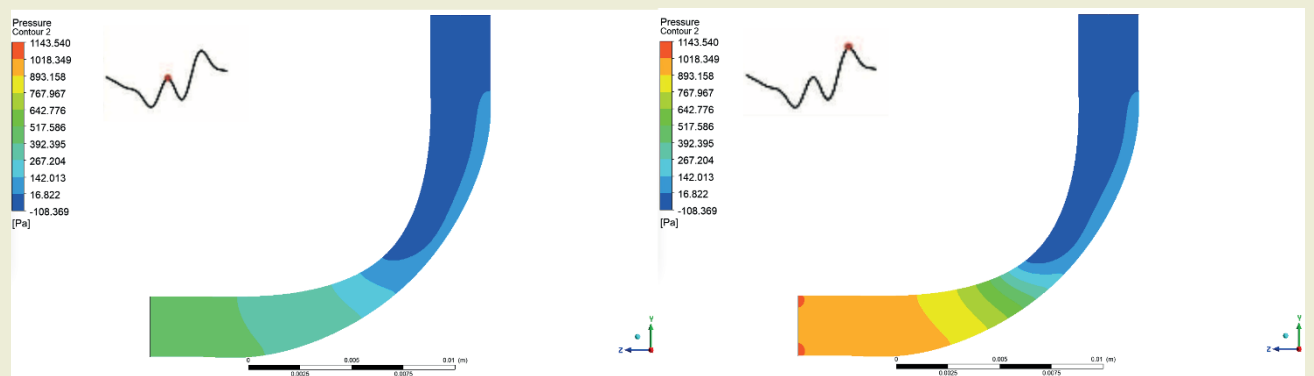


Figure 27. Pressure contour of systole (left) and diastole (right) with 40% stenosis.

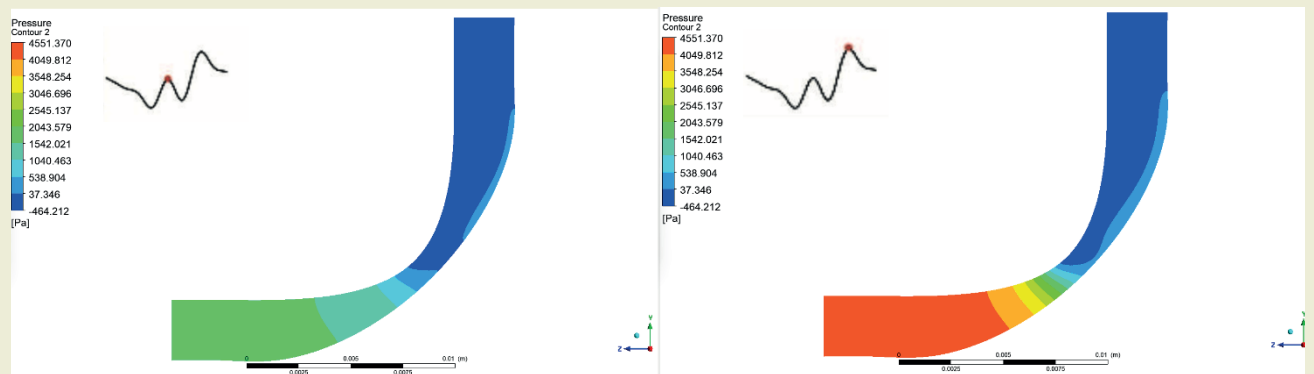


Figure 28. Pressure contour of systole (left) and diastole (right) with 60% stenosis.

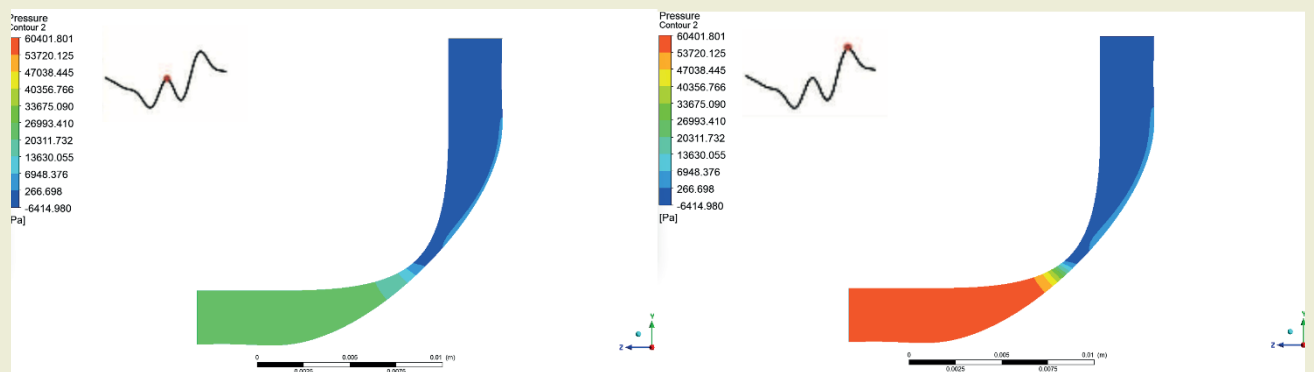


Figure 29. Pressure contour of systole (left) and diastole (right) with 80% stenosis.

3.1-3 WSS contours for different curvatures and stenoses

A] WSS contour of 30-degree curvature

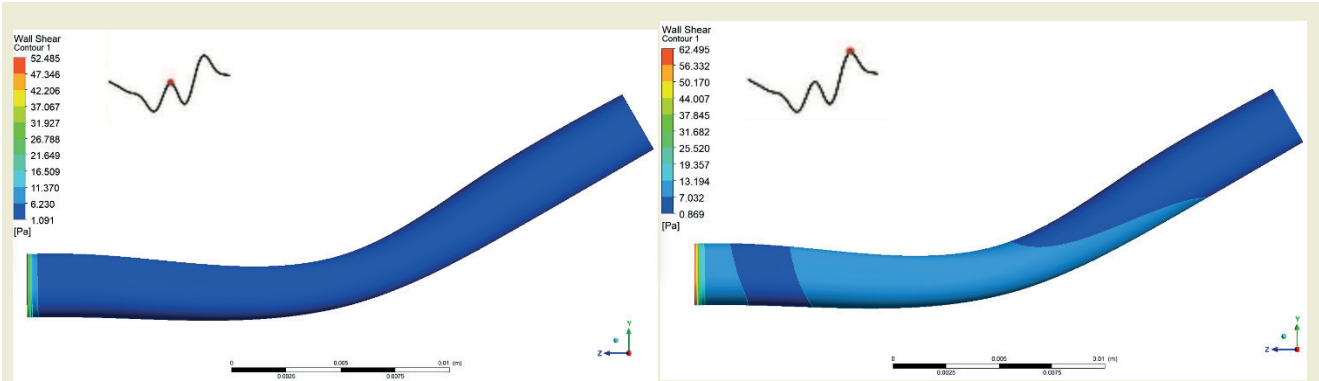


Figure 30. Wall shear stress (WSS) contour of systole (left) and diastole (right) with 20% stenosis.

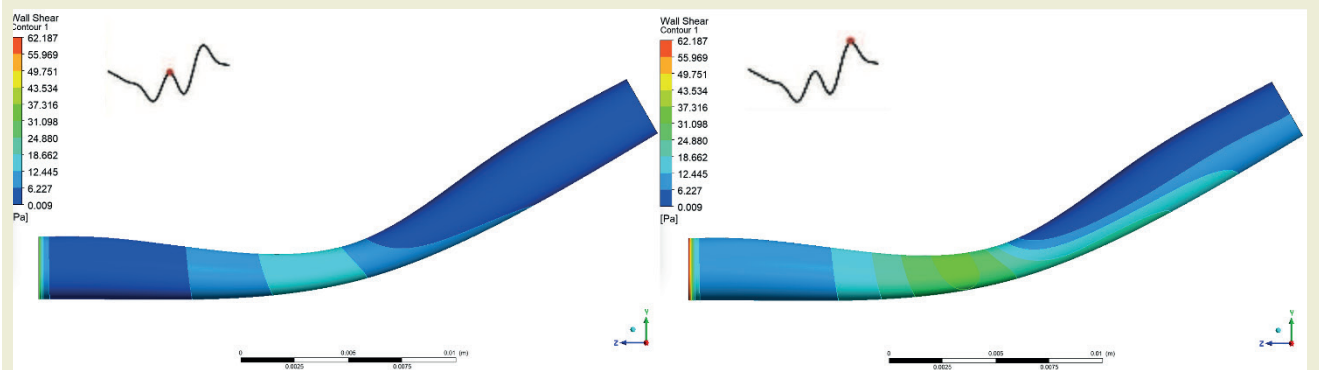


Figure 31. Wall shear stress (WSS) contour of systole (left) and diastole (right) with 40% stenosis.

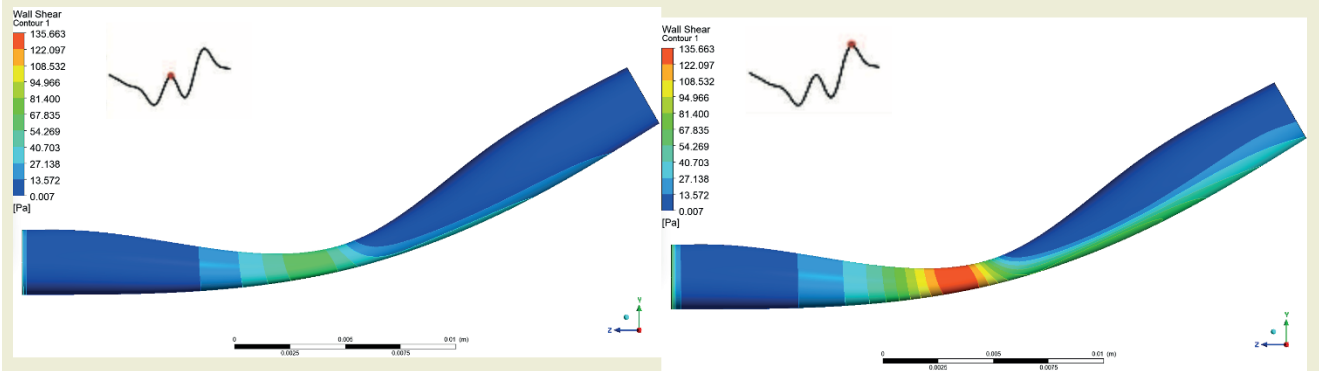


Figure 32. Wall shear stress (WSS) contour of systole (left) and diastole (right) with 60% stenosis.

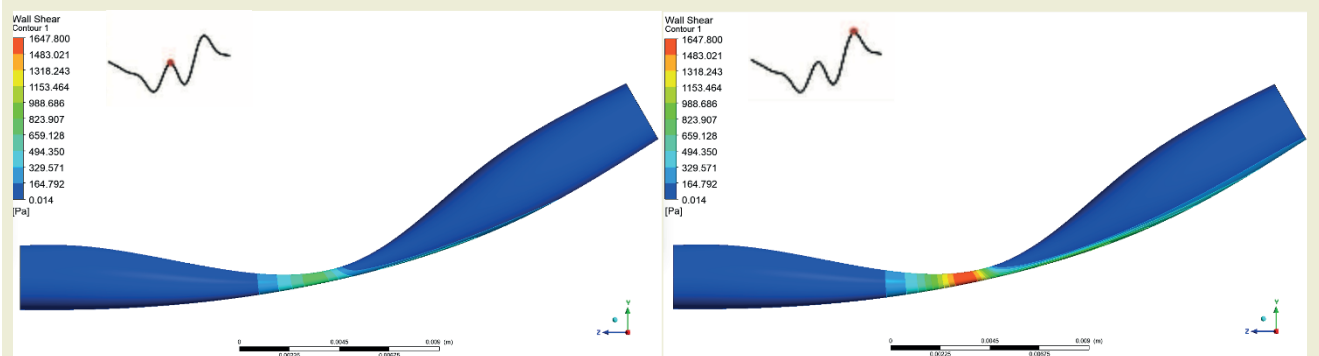


Figure 33. Wall shear stress (WSS) contour of systole (left) and diastole (right) with 80% stenosis.

B] WSS contour of 60-degree curvature

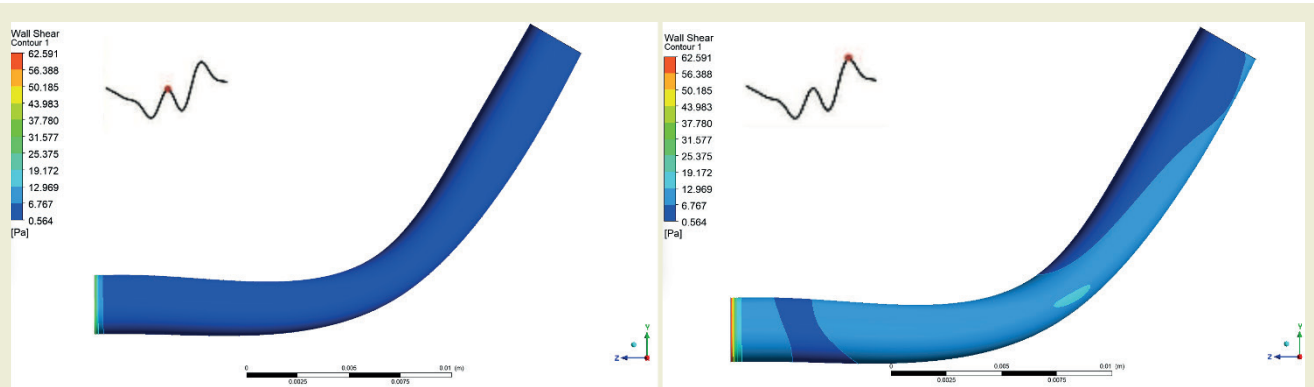


Figure 34. Wall shear stress (WSS) contour of systole (left) and diastole (right) with 20% stenosis.

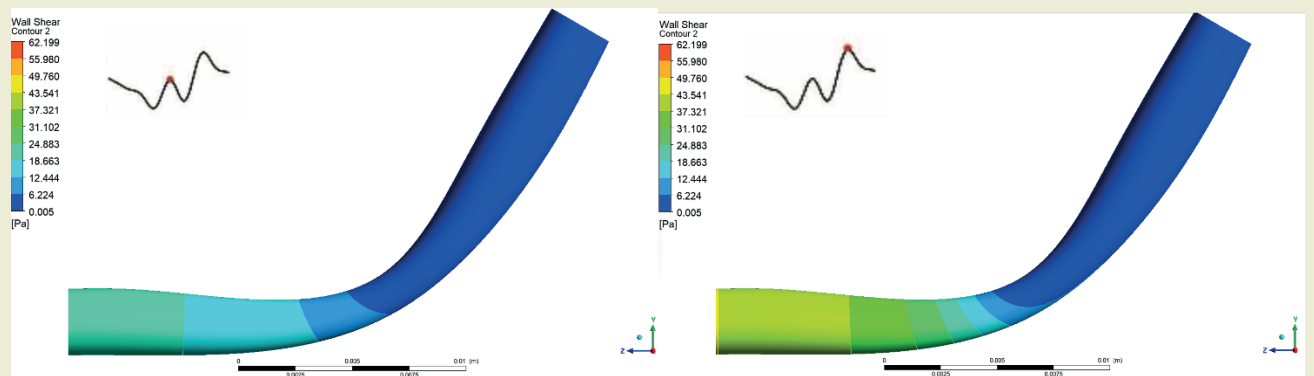


Figure 35. Wall shear stress (WSS) contour of systole (left) and diastole(right) with 40% stenosis.

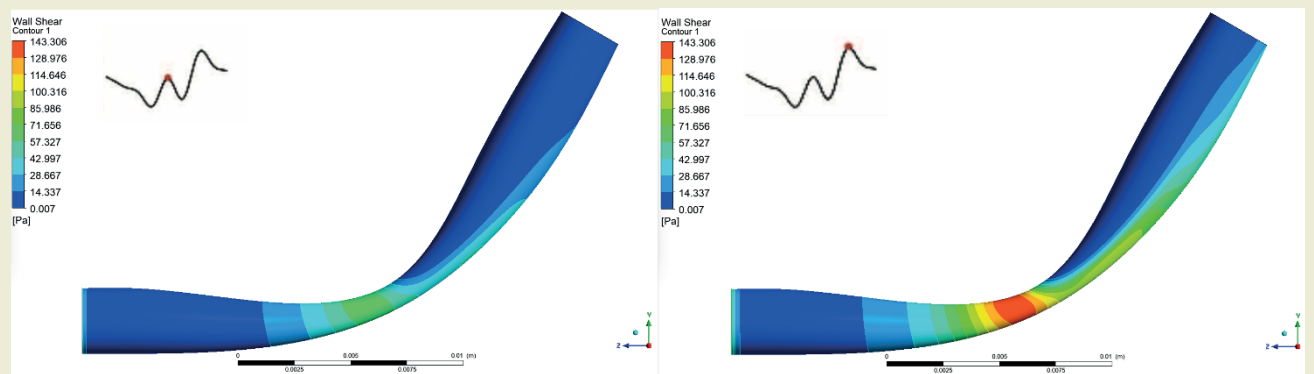


Figure 36. Wall shear stress (WSS) contour of systole (Left) and Diastole(right) with 60% stenosis.

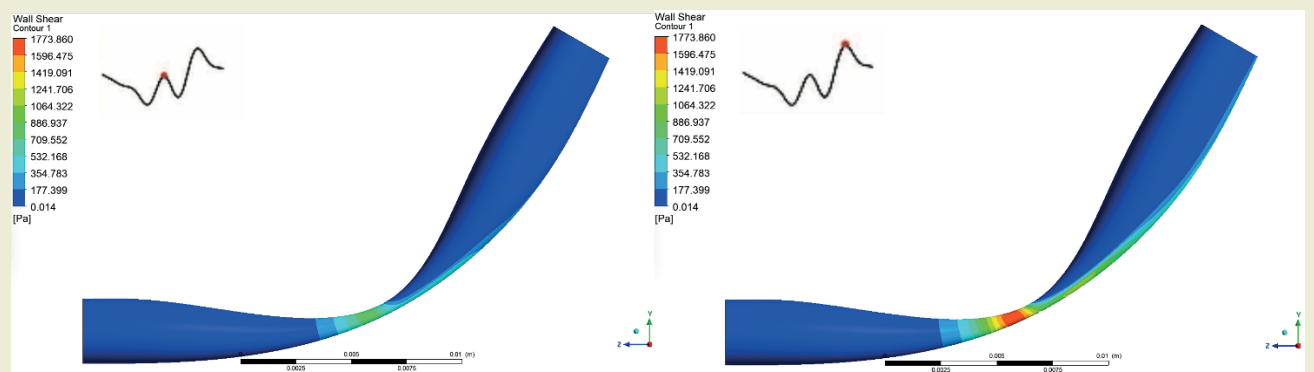


Figure 37. Wall shear stress (WSS) contour of systole (left) and diastole (right) with 80% stenosis.

C] WSS contour of 90-degree curvature

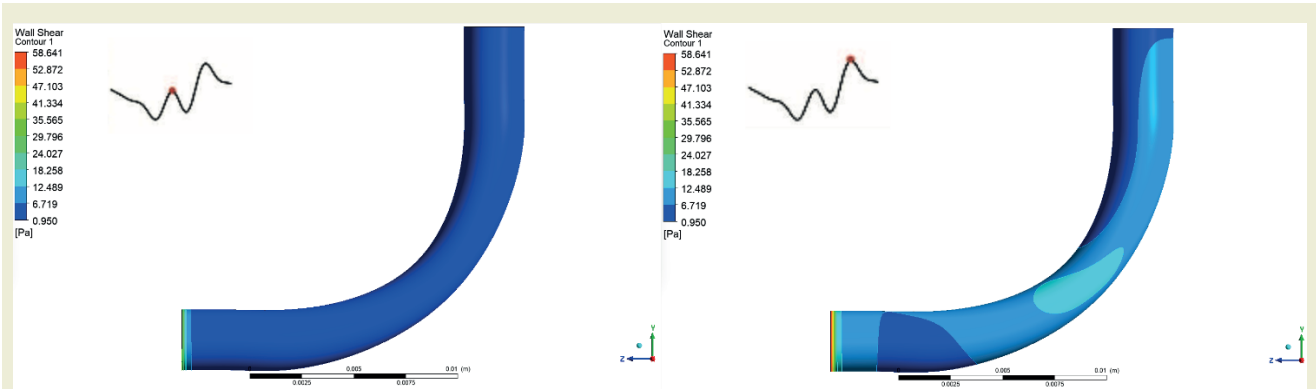


Figure 38. Wall shear stress (WSS) contour of systole (left) and diastole (right) with 20% stenosis.

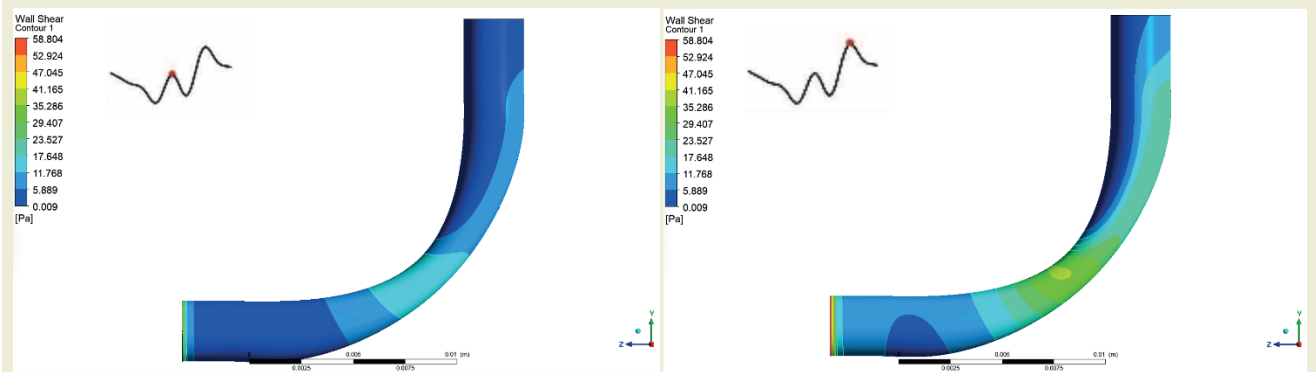


Figure 39. Wall shear stress (WSS) contour of systole (left) and diastole (right) with 40% stenosis.

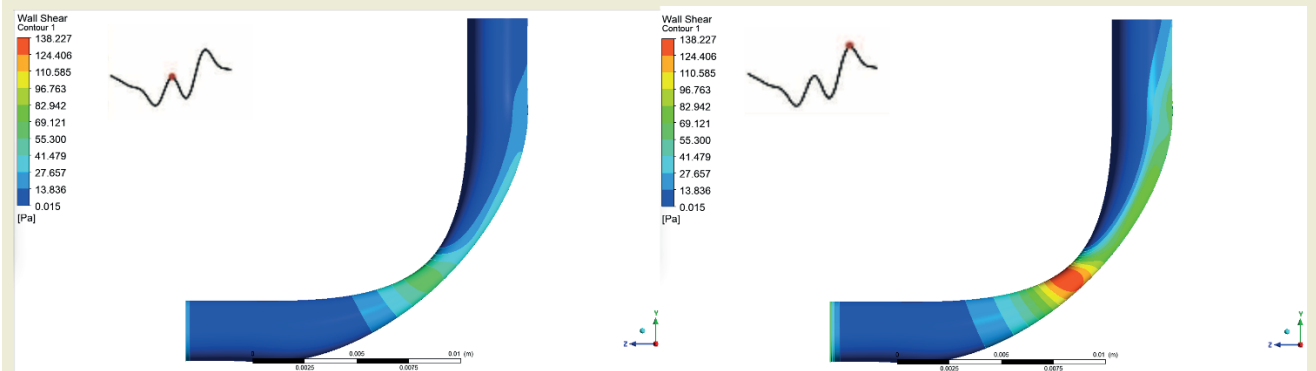


Figure 40. Wall shear stress (WSS) contour of systole (left) and diastole (right) with 60% stenosis.

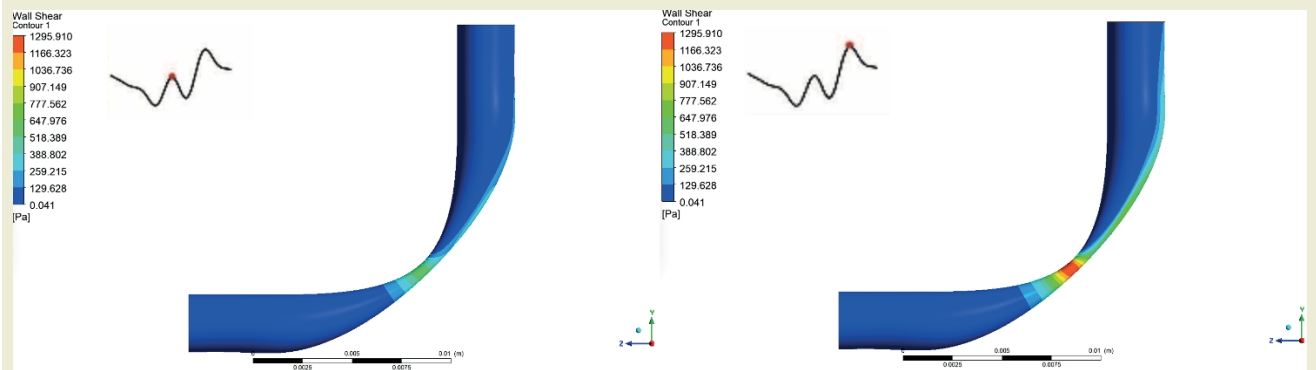


Figure 41. Wall shear stress (WSS) contour of systole (left) and diastole (right) with 80% stenosis.

3.1-4 Velocity vector contour plots for different curvatures and stenoses

A) Velocity vector plot of 30-degree curvature

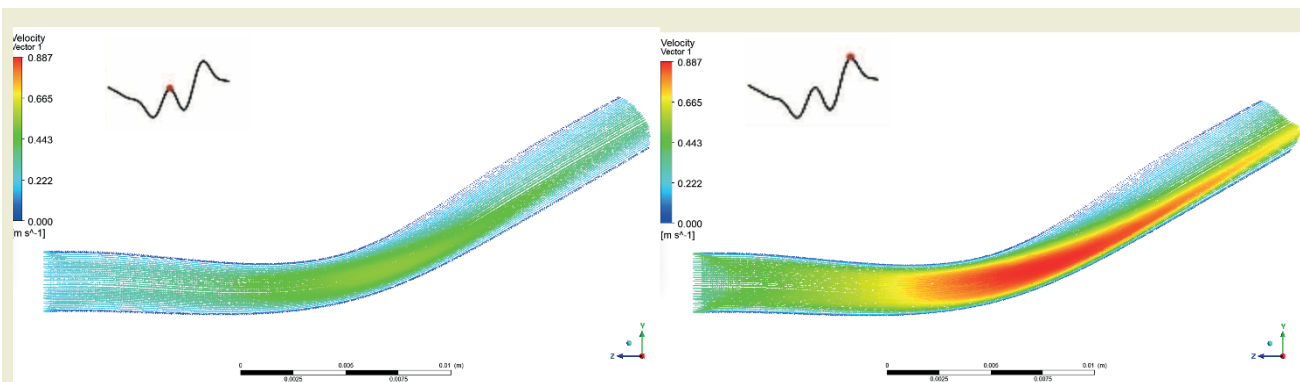


Figure 42. Velocity vector plot of systole (left) and diastole (right) with 20% stenosis.

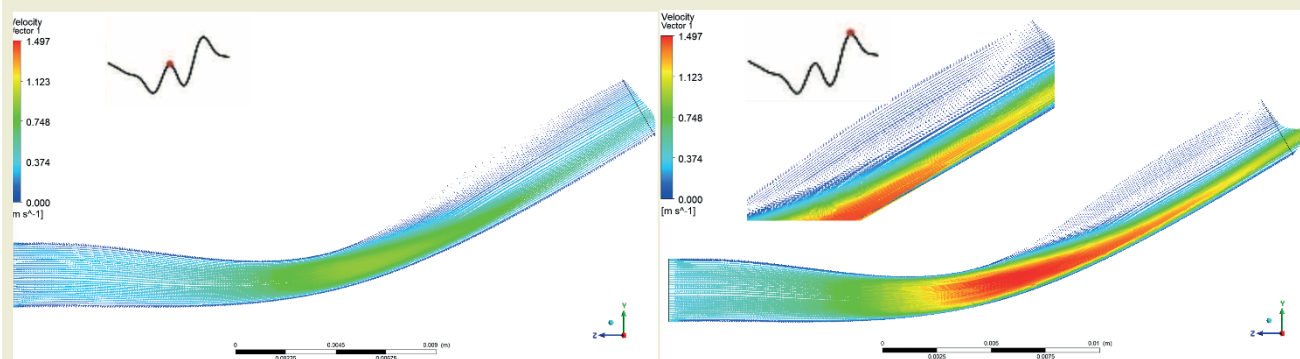


Figure 43. Velocity vector plot of systole (left) and diastole (right) with 40% stenosis.

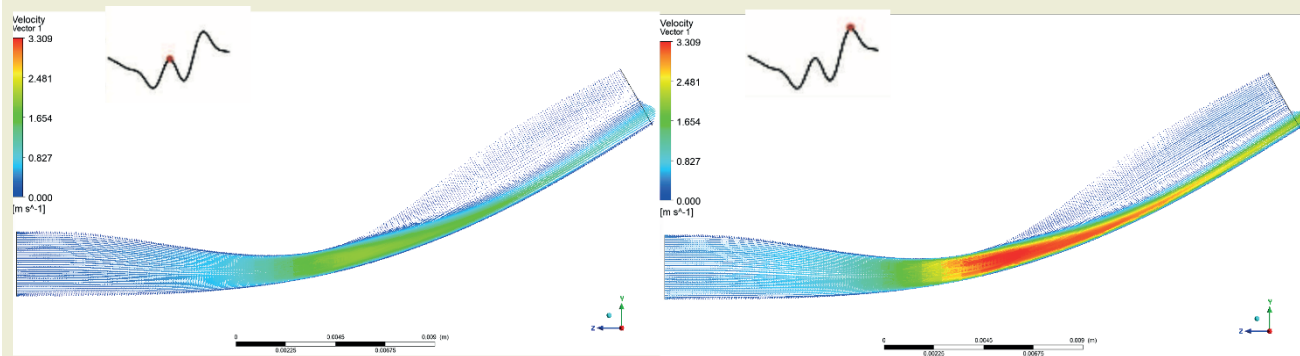


Figure 44. Velocity vector plot of systole (left) and diastole (right) with 60% stenosis.

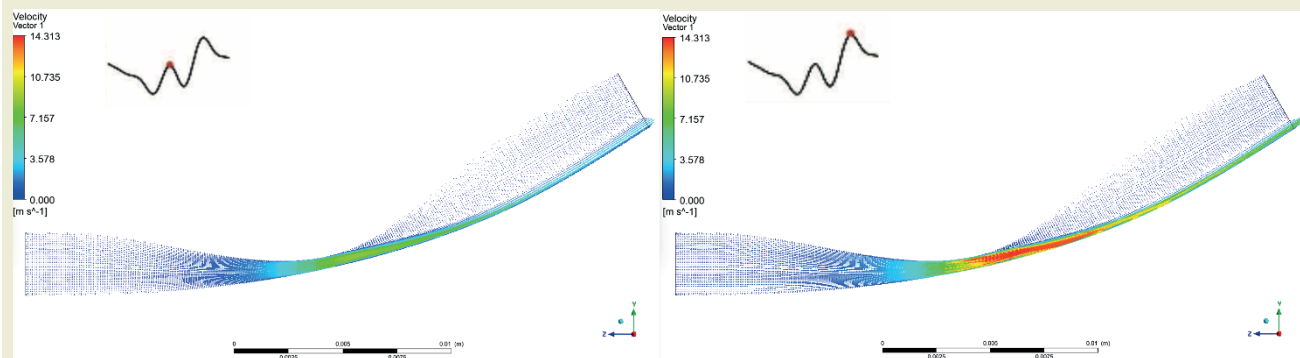


Figure 45. Velocity vector plot of systole (left) and diastole (right) with 80% stenosis.

B] Velocity vector plot of 30-degree curvature

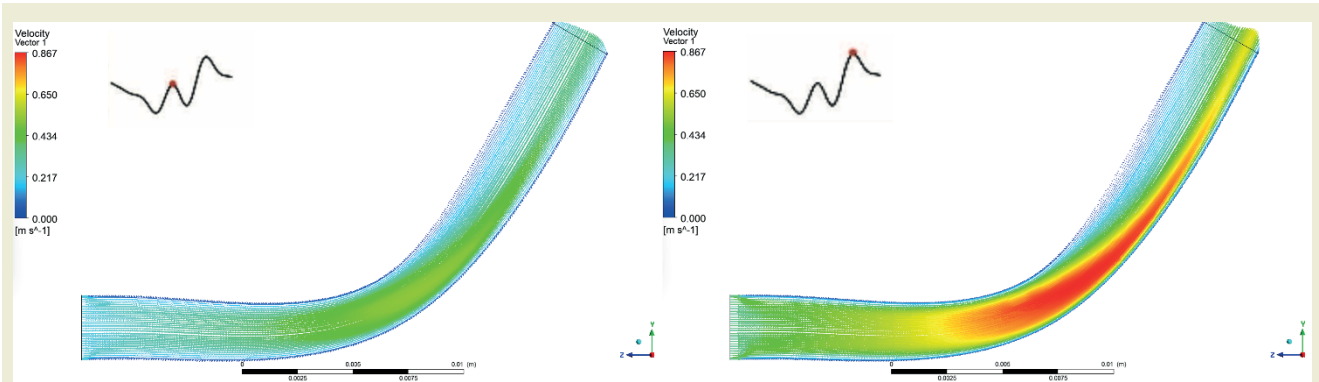


Figure 46. Velocity vector plot of systole (left) and diastole (right) with 20% stenosis.

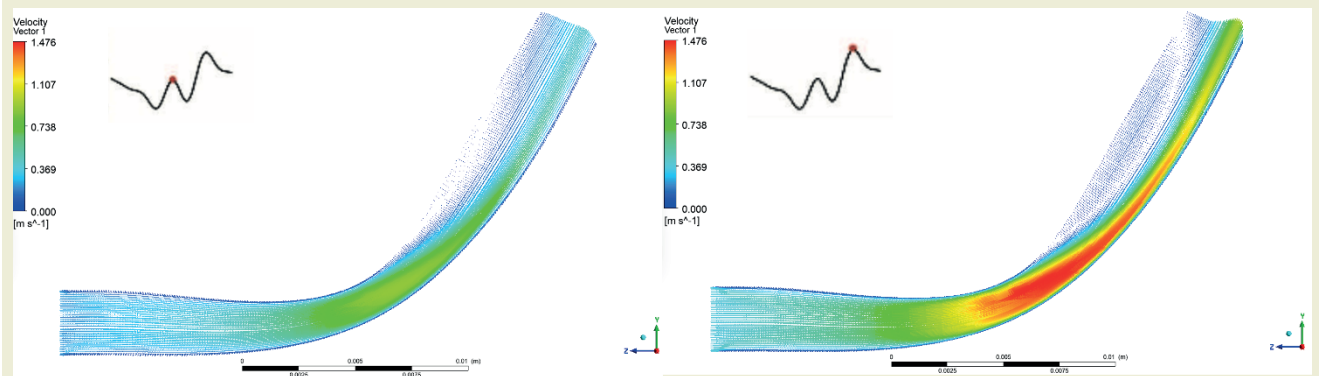


Figure 47. Velocity vector plot of systole (left) and diastole (right) with 40% stenosis.

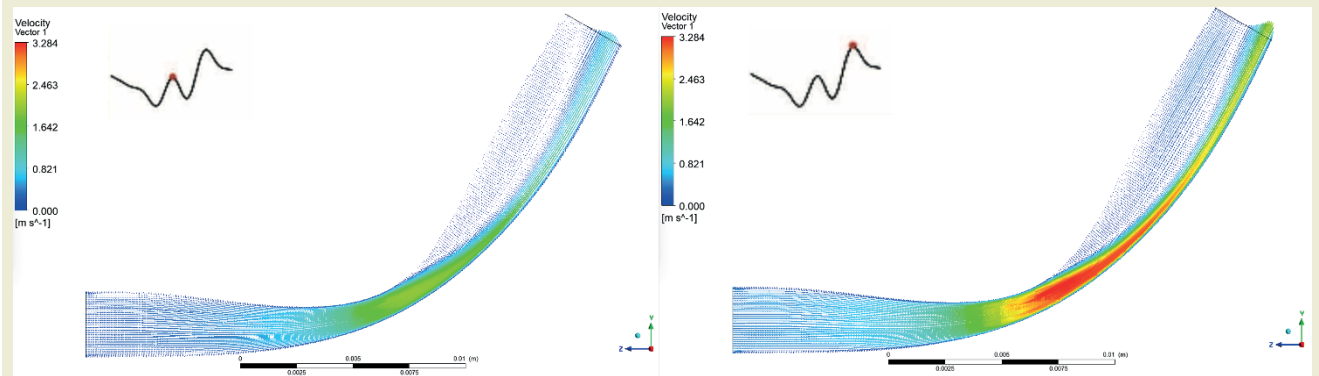


Figure 48. Velocity vector plot of systole (left) and diastole (right) with 60% stenosis.

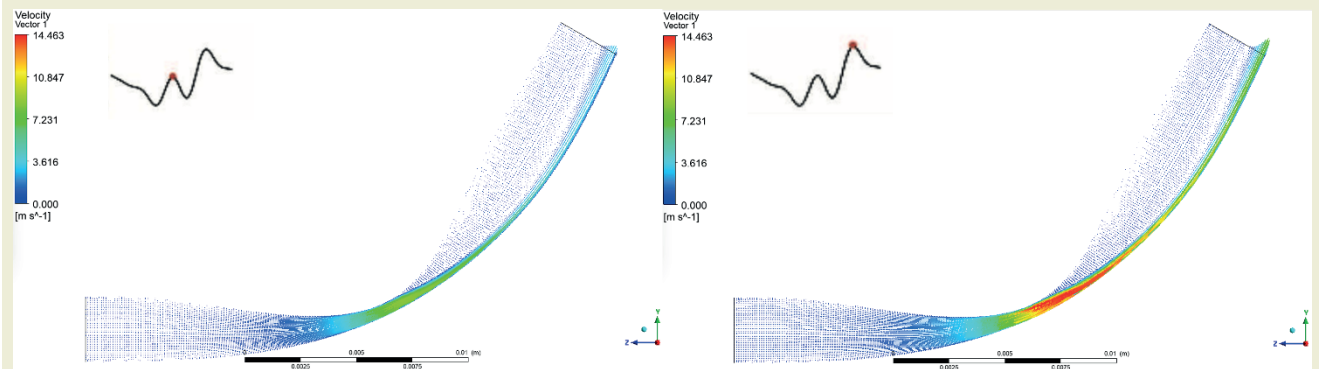


Figure 49. Velocity vector plot of systole (left) and diastole (right) with 80% stenosis.

C] Velocity vector plot of 90-degree curvature

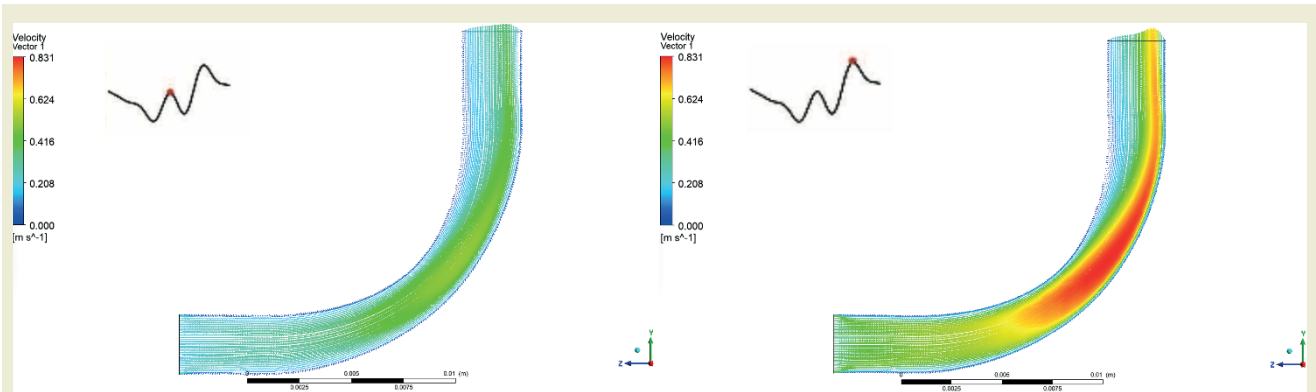


Figure 50. Velocity vector plot of systole (left) and diastole (right) with 20% stenosis.

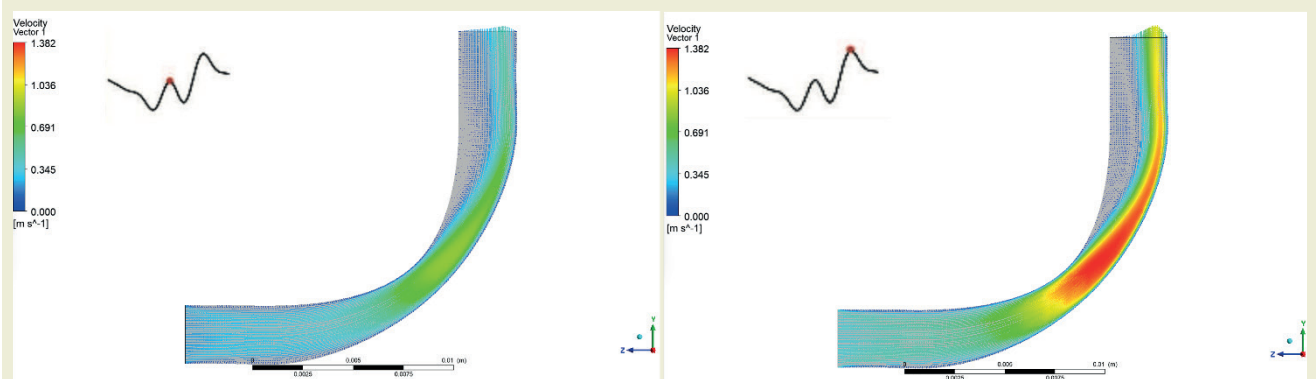


Figure 51. Velocity vector plot of systole (left) and diastole (right) with 40% stenosis.

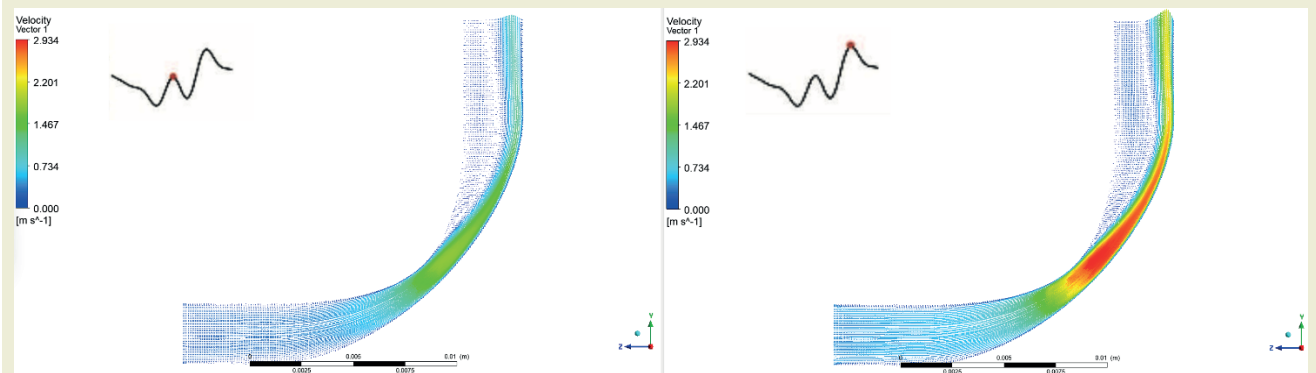


Figure 52. Velocity vector plot of systole (left) and diastole (right) with 60% stenosis.

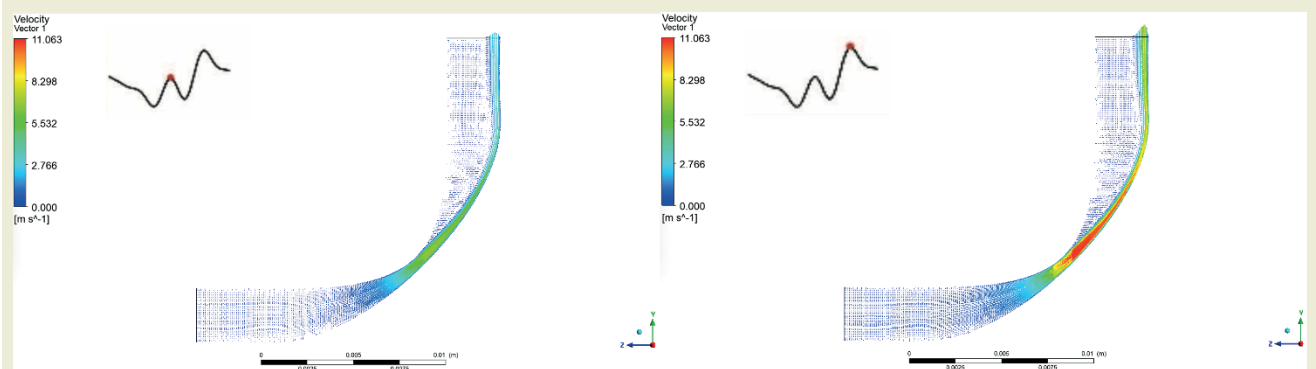


Figure 53. Velocity vector plot of systole (left) and diastole (right) with 80% stenosis.

3.2. FSI (arterial stress and deformation) Visualizations

Next, we present the structural (stress) results, for Von Mises stress and total deformation (displacement) of

the artery structure, again for 3 curvature cases (30, 60, 90 degrees) each with 4 stenosis depths (20, 40, 60, 80%). The results are therefore grouped in 12 sets in 2 subsections (A, B). In each figure we provide 2 graphs, one for the systole and the other for the diastole.

3.2-1 Von Mises stress contour plots for different curvatures and stenoses

A] Von Mises stress contour of 30-degree curvature

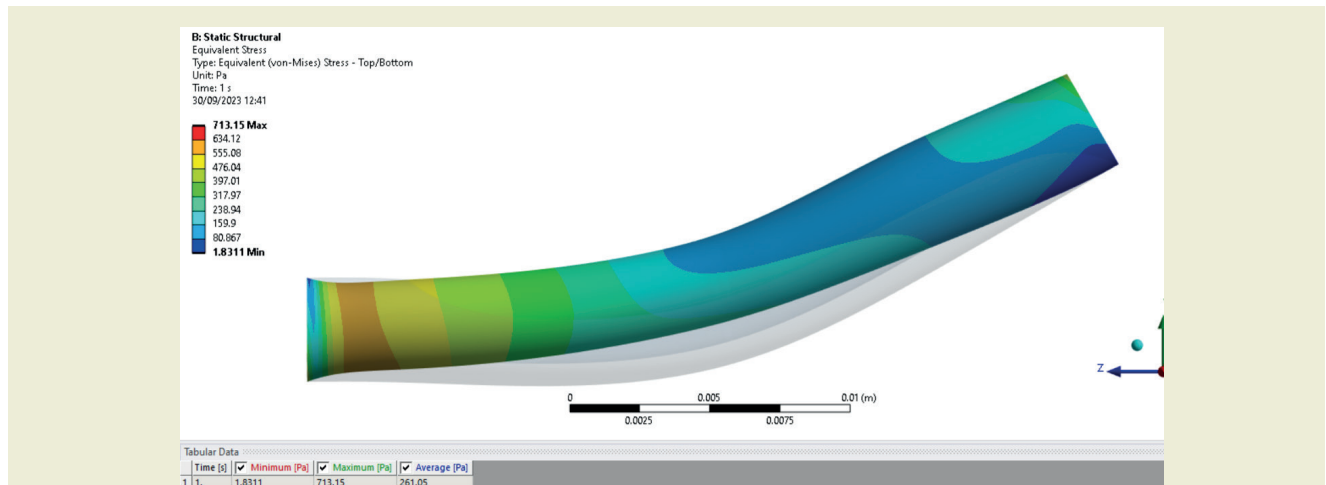


Figure 54. Von Mises stress of artery with 20% stenosis.

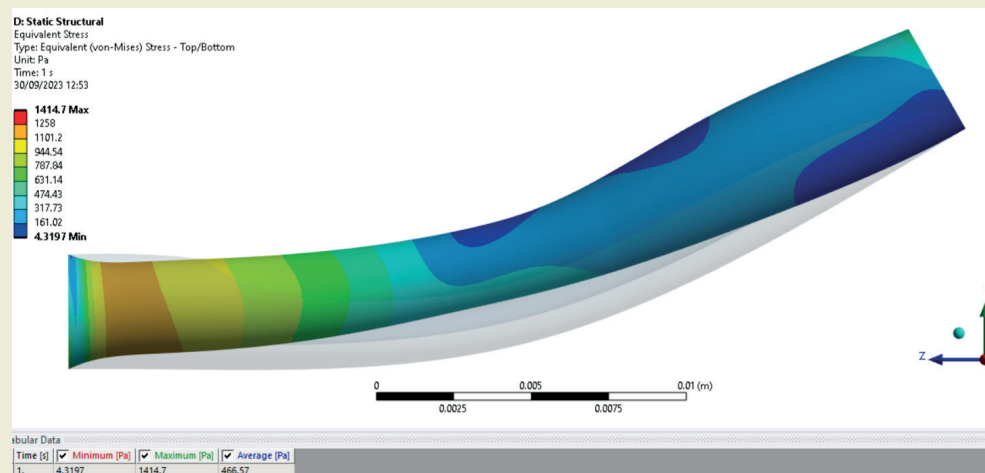


Figure 55. Von Mises stress of artery with 40% stenosis.

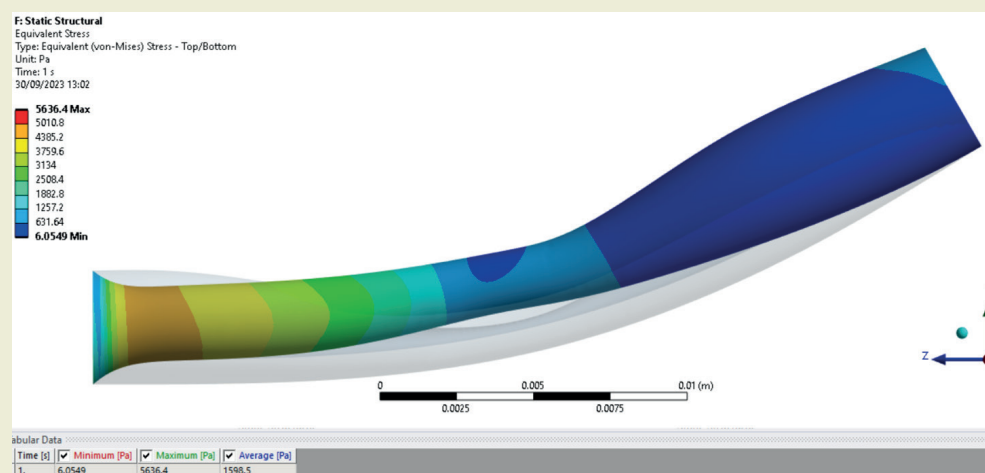


Figure 56. Von Mises stress of artery with 60% stenosis.

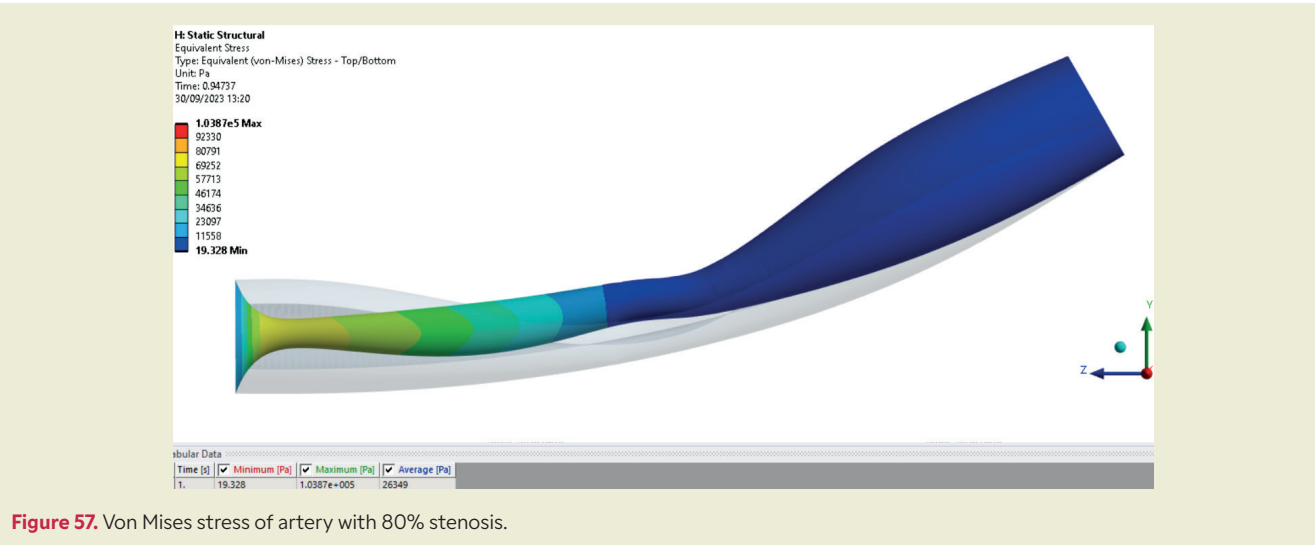


Figure 57. Von Mises stress of artery with 80% stenosis.

B] Von Mises stress contour of 60-degree curvature

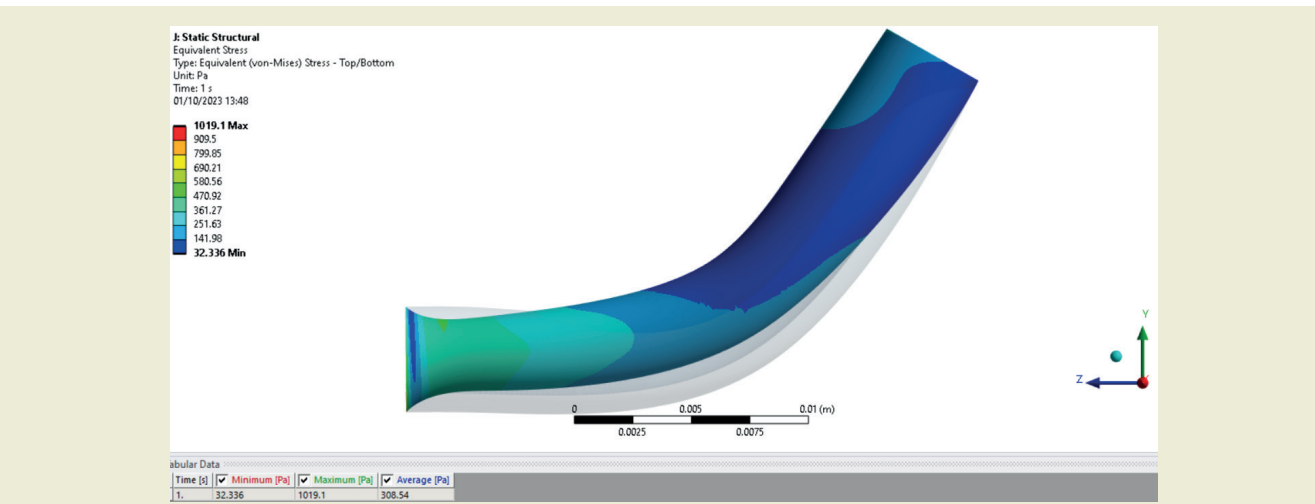


Figure 58. Von Mises stress of artery with 20% stenosis.

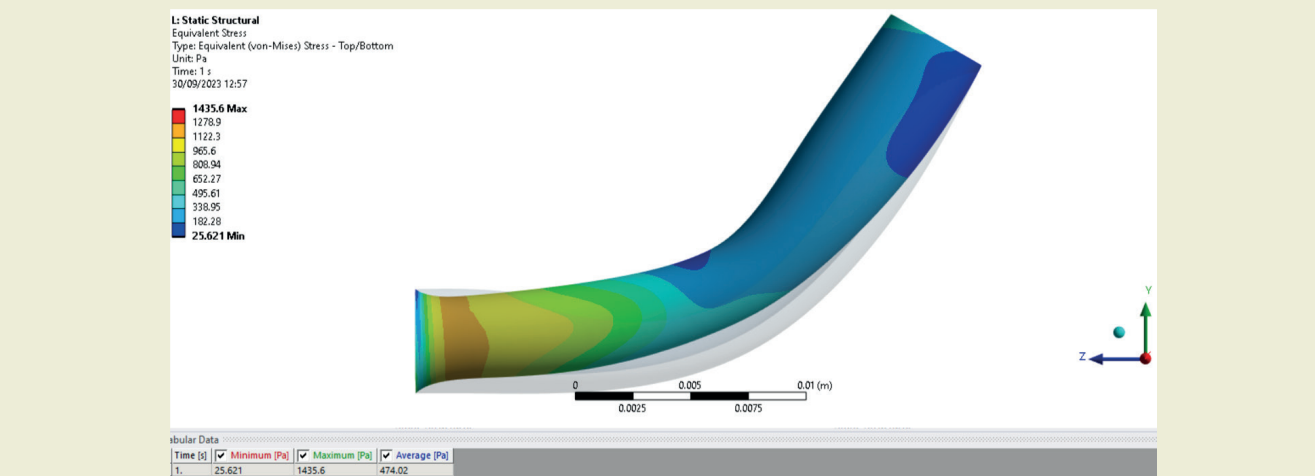


Figure 59. Von Mises stress of artery with 40% stenosis.

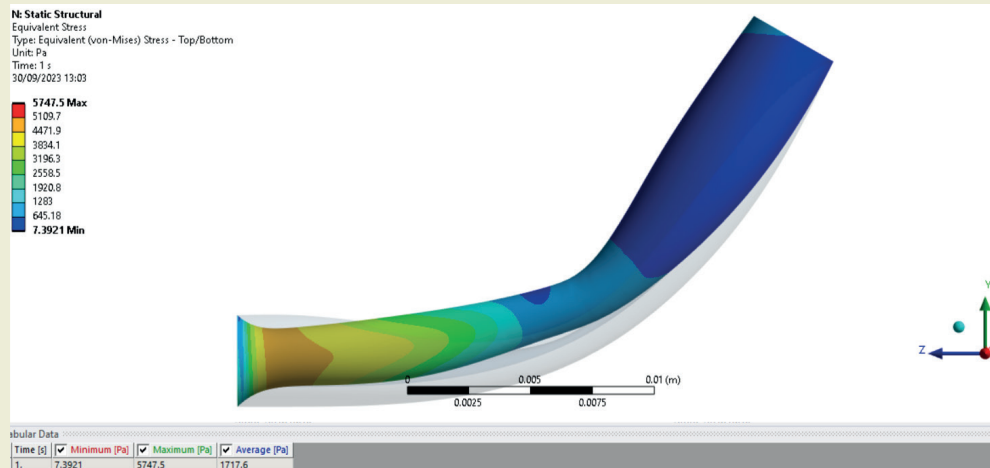


Figure 60. Von Mises stress of artery with 60% stenosis.

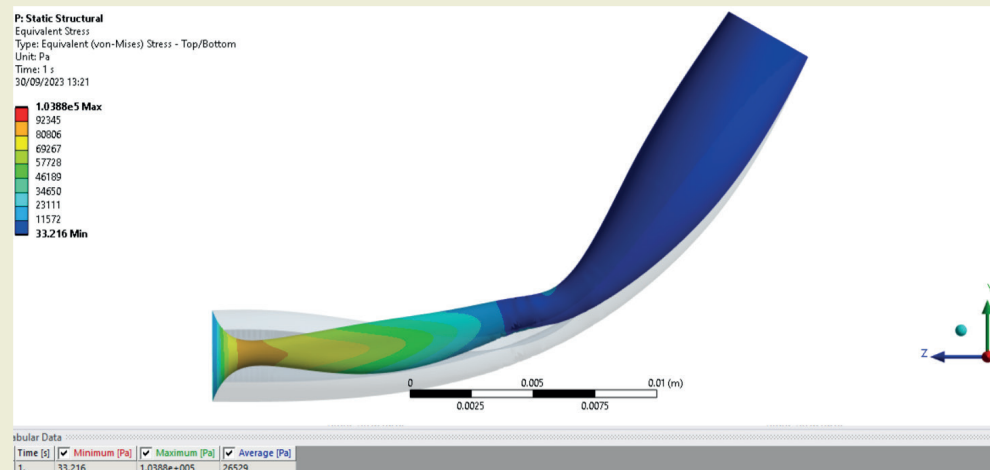


Figure 61. Von Mises stress of artery with 80% stenosis.

C) Von Mises stress contour of 90-degree curvature

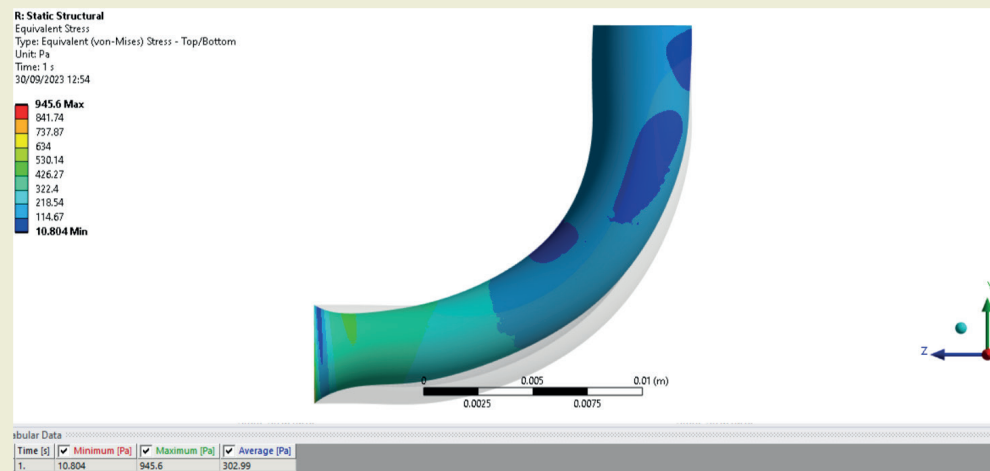


Figure 62. Von Mises stress of artery with 20% stenosis.

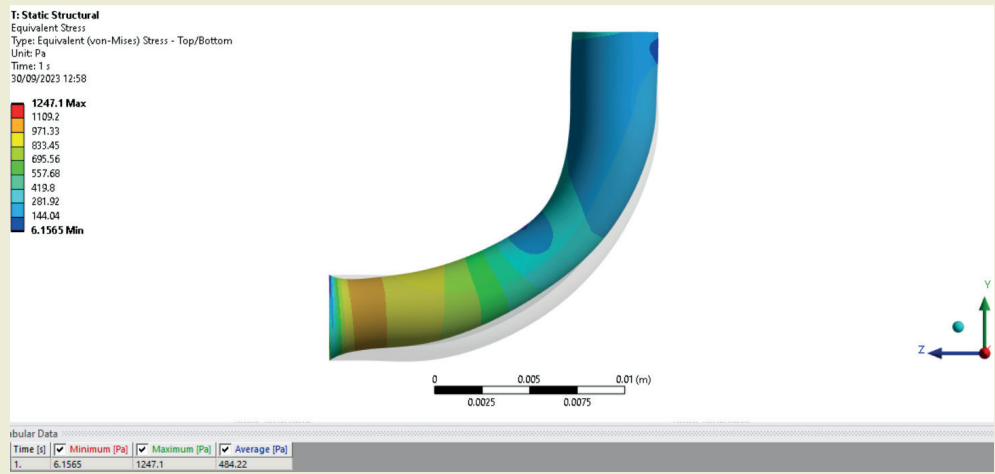


Figure 63. Von Mises stress of artery with 40% stenosis.

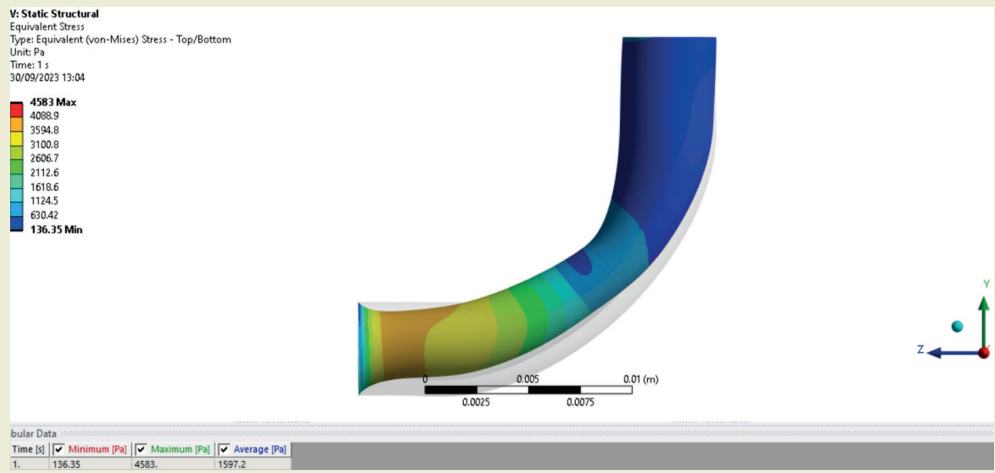


Figure 64. Von Mises stress of artery with 60% stenosis.

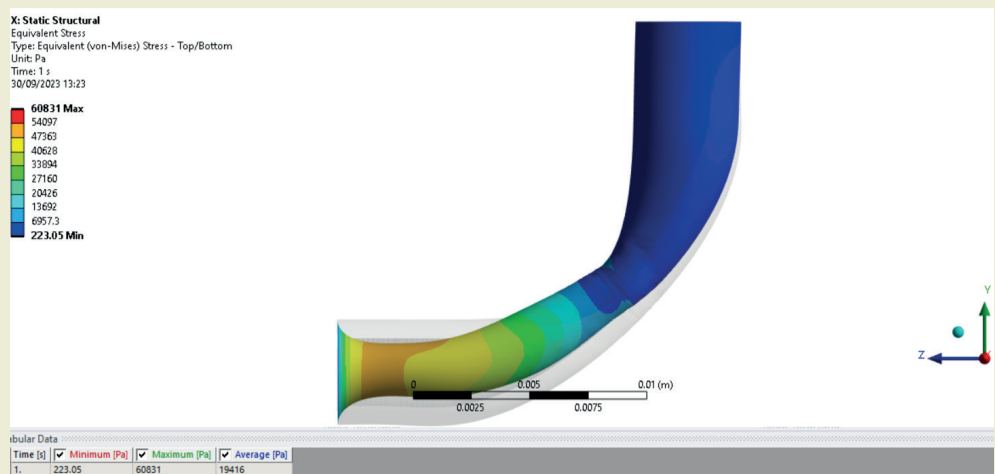


Figure 65. Von Mises stress of artery with 80% stenosis.

3.2-2 Total displacement (deformation) contour plots for different curvatures and stenoses

A) Total displacement contour of 30-degree curvature

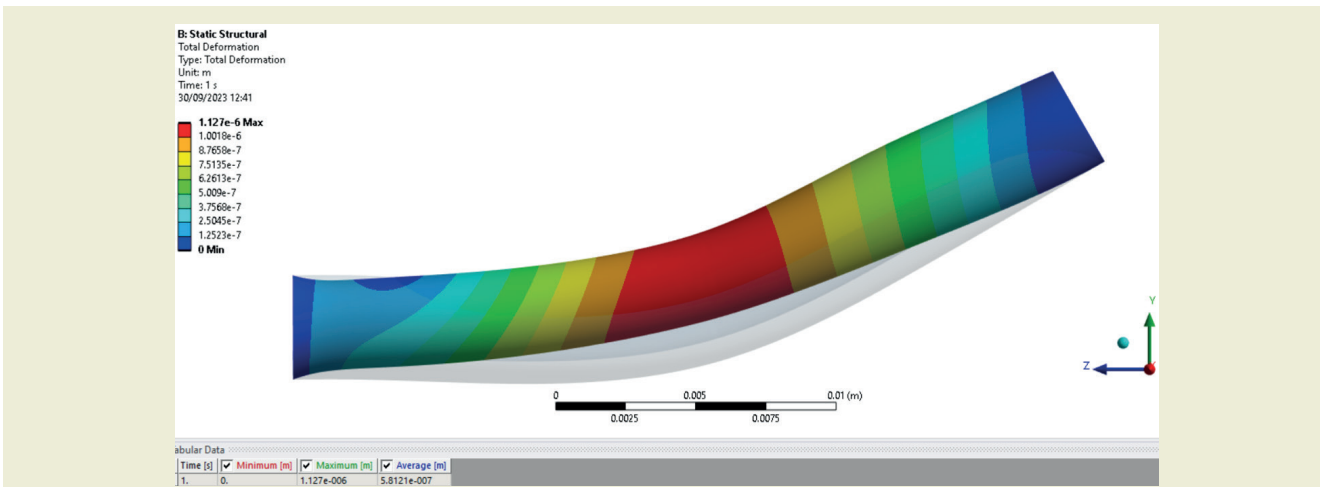


Figure 66. Total displacement of artery with 20 % stenosis.

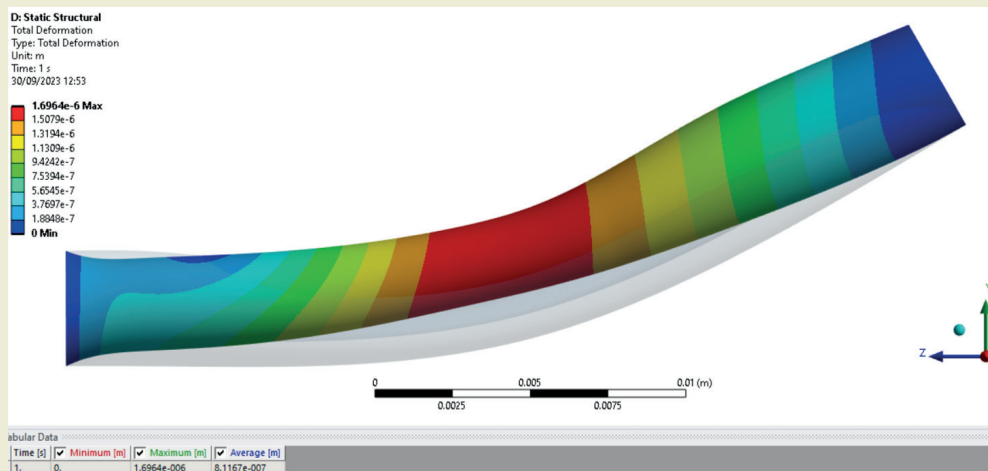


Figure 67. Total displacement of artery with 40% stenosis.

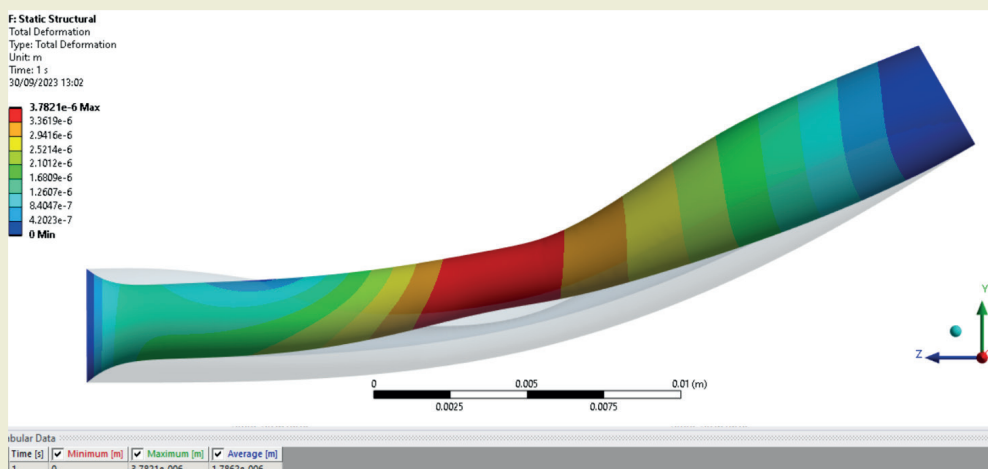


Figure 68. Total displacement of artery with 60% stenosis.

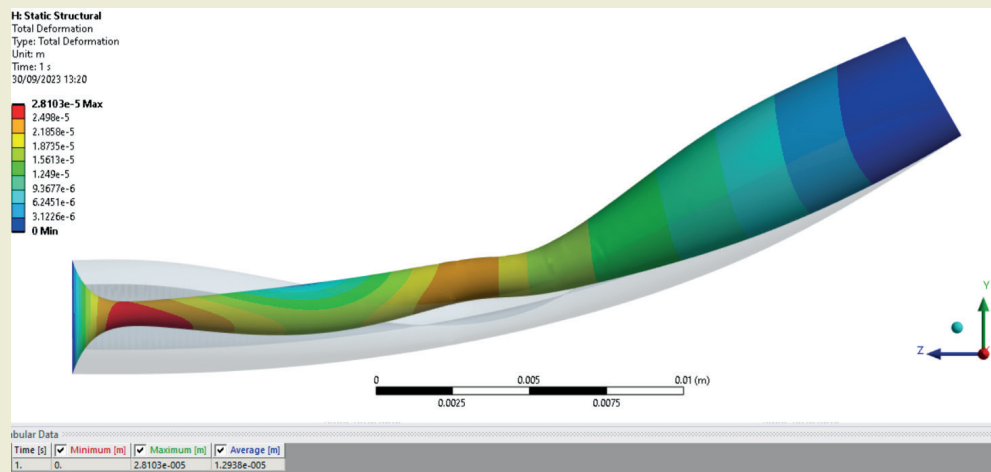


Figure 69. Total displacement of artery with 80 % stenosis.

B] Total displacement contour of 60-degree curvature

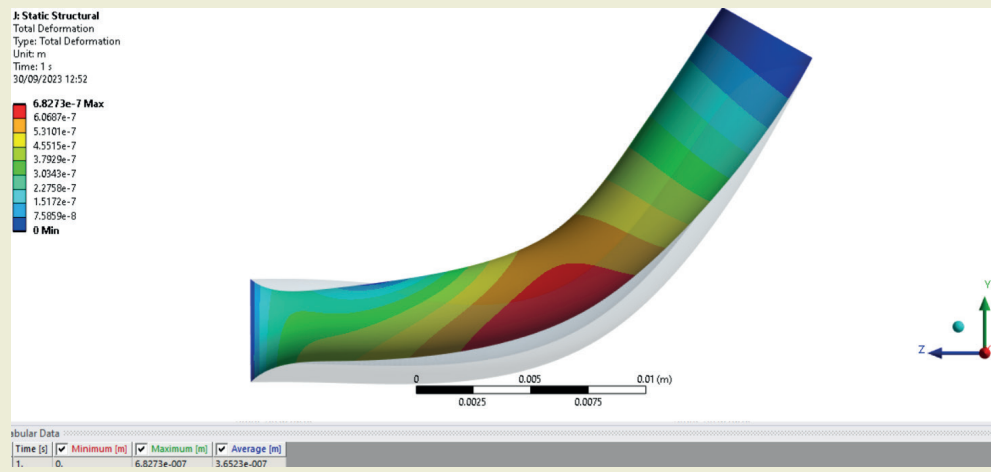


Figure 70. Total displacement of artery with 20 % stenosis.

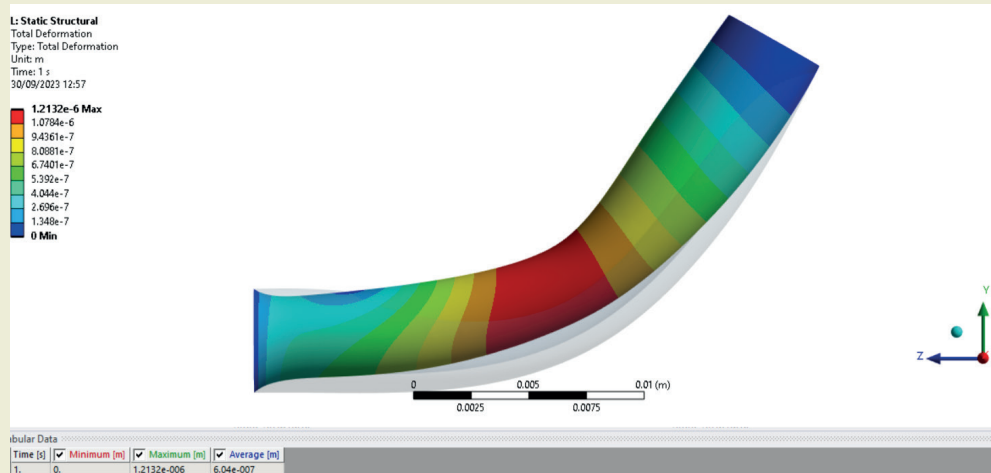


Figure 71. Total displacement of artery with 40 % stenosis.

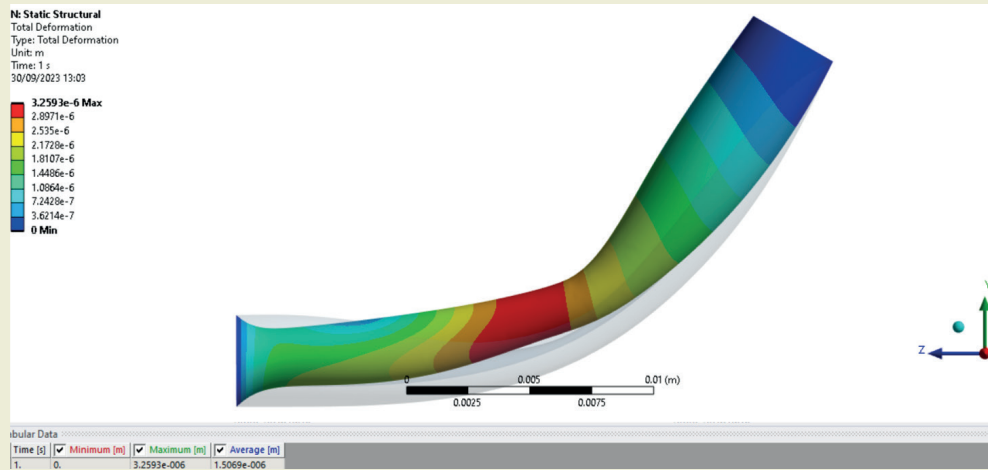


Figure 72. Total displacement of artery with 60 % stenosis.

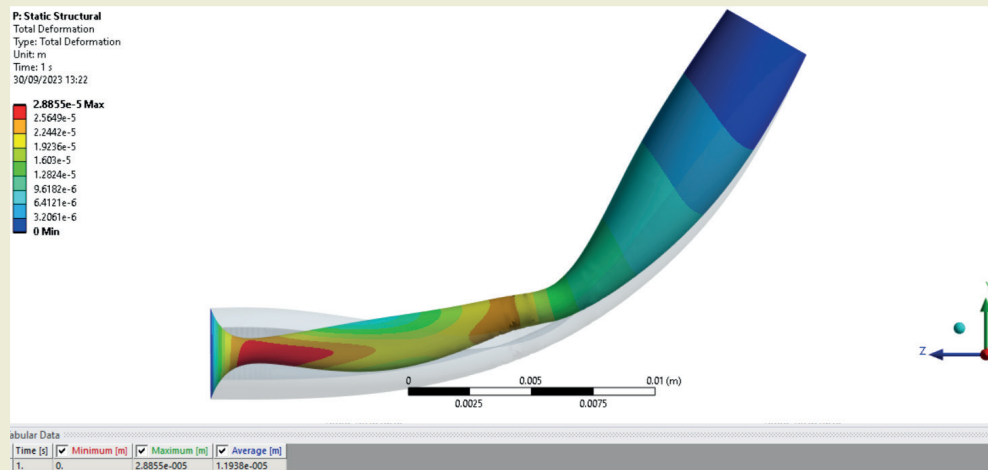


Figure 73. Total displacement of artery with 80 % stenosis.

C) Total displacement contour of 90-degree curvature

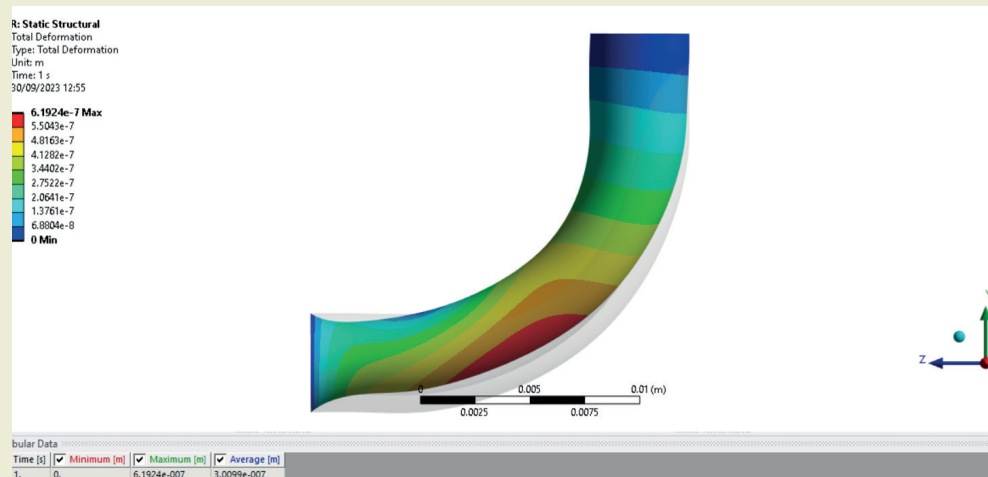


Figure 74. Total displacement of artery with 20 % stenosis.

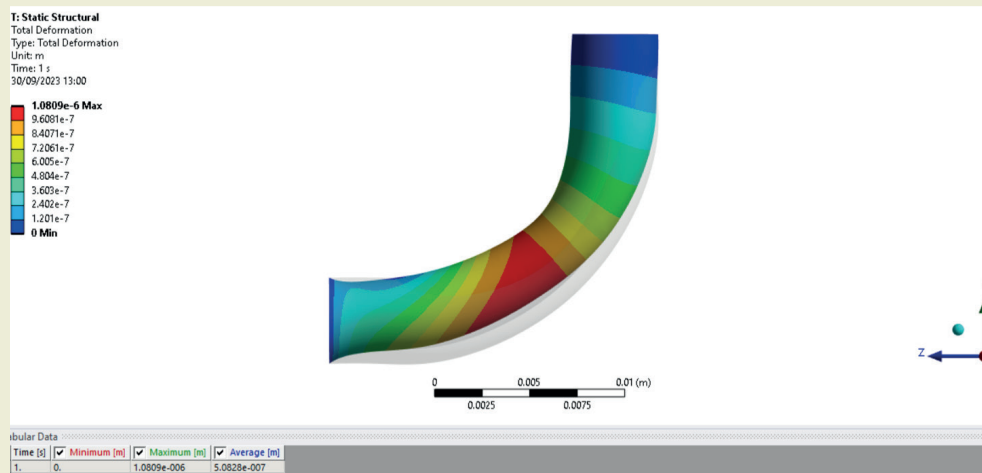


Figure 75. Total displacement of artery with 40 % stenosis.

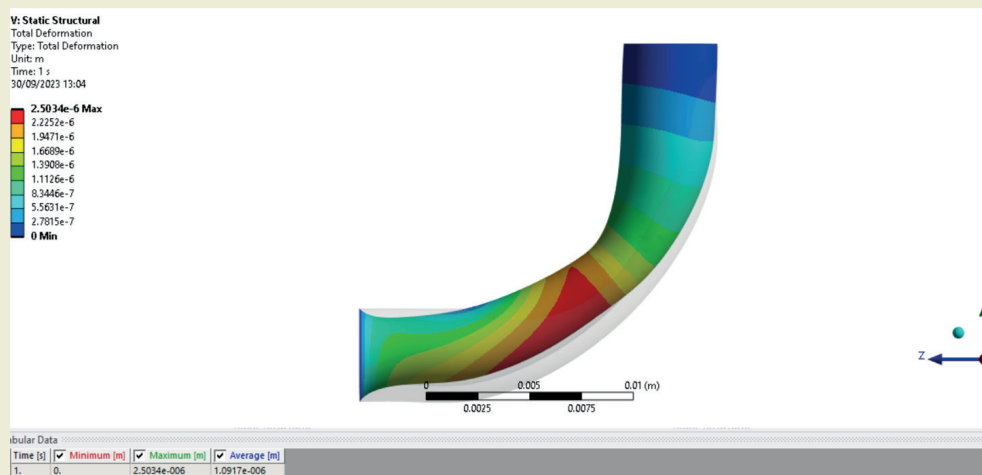


Figure 76. Total displacement of artery with 60 % stenosis.

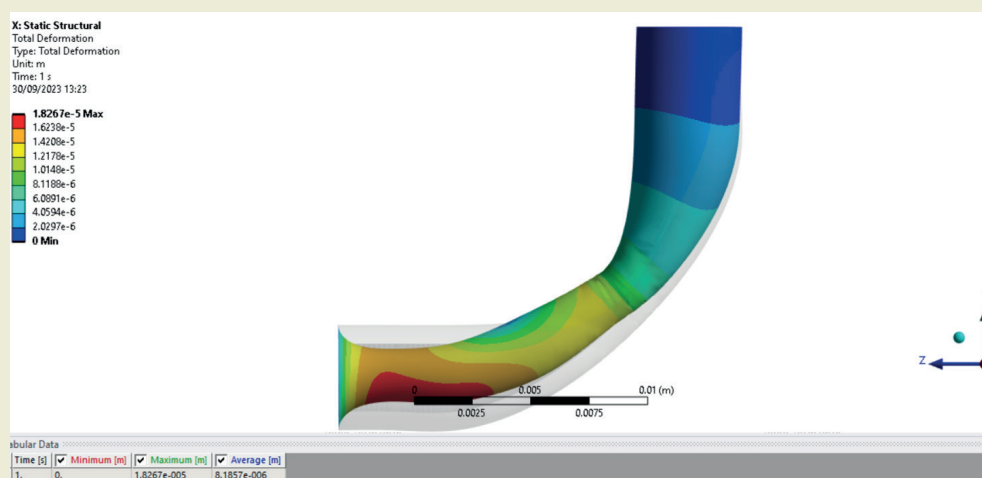


Figure 77. Total displacement of artery with 80 % stenosis.

4. Discussion

Inspection of the CFD results as depicted in ►Figures 6-17, i.e. velocity contours, for the three sets of curvatures considered (30, 60, 90 degrees), the estimated velocity profiles are different both in systole (0.4s) and diastole (0.8s) and are significantly modified by both curvature and stenosis depth (percentage). Velocity is clearly much higher in the diastole compared to the systole for all cases. This is due to the compression in the artery by the contraction of the myocardium during systole, therefore, most of the blood flow occurs during diastole, increasing the blood flow. The maximum velocity is noted at the throat area (stenosis) and slowly reduces as it reaches the outlet. The velocity also changes when compared with different percentages of stenosis. The velocity magnitude increases as the percentage of stenosis increases; however larger high velocity zones are computed for the 40% case (red area) relative to other stenosis depths. The variation in the post-stenotic region is quite apparent and is exacerbated with greater curvature and larger stenosis depths. The blue low velocity zones far downstream from the stenosis significantly expand with greater stenosis for the low curvature cases (30 degrees); a similar effect is observed for the other two curvature cases. The low entry velocity zones (blue) are also very evident for the 30 and 60-degree curvature cases at all stenotic depths; however, for the 90-degree bend case, much greater velocities precede the stenosis region at least up to a stenotic depth of 40%. However, with subsequent increment in the stenosis to 60% and 80% (►Figures 16 and 17) the blue deceleration zones dominate, and the red high acceleration zone is progressively constricted in the vicinity of the outer curved wall. Poiseuille's law implies that the flow rate is highly dependent on the radius. In an artery without stenosis, the pressure gradient increases due to an increase in flow rate. However, this is not the case with the presence of a stenosis. The narrowing of the artery causes additional pressure modifications. This can be described as a quadratic polynomial. At some point, the pressure coefficient is independent of flow rate in higher flow rates. Then, it is dependent on the degree of stenosis. The velocity is higher at the outer curvature of the wall when compared with the inner side of the artery downstream. This indicates the pressure drops at the stenosis area and creates zones of low pressure, contracting the artery and forcing blood to accelerate. The flow also increases in speed even before reaching the throat area, as noted by Ku [3]. Since non-Newtonian (Carreau) blood is considered the shear rate and viscosity differs from conventional Newtonian blood flow simulations. The velocity contours (streamlines) are therefore different also. Inspection of the pressure contour plots in ►Figures 18-29 (again for all three curvature cases with 4 stenotic depths per case) demonstrates that the pressure is generally much higher upstream of the stenosis when compared to the downstream. The local pressure drop after the flow passes through stenosis is attributable to the constriction which induces accelera-

tion but by virtue of Bernoulli's equation, manifests in a pressure slump. The pressure drops further with the flow rate increase, the pressure difference is elevated as the stenosis is increased.

Since stenosis is responsible for restricting the flow, a larger wall shear stress (WSS) magnitude is induced at the throat. The WSS predicted along the artery wall are compared in ►Figures 30-41, again for the three curvature cases with 4 different stenotic depths. Apparently in all scenarios low wall shear stress arises at the entry zone (pre-stenotic) and again in the exit zone (post-stenotic), although initially for the 30 degrees curvature at low stenosis there is a higher wall shear stress immediately at the entry. However, the high WSS is identified generally along the stenosis throat zone indicating that flow acceleration here produces faster shearing in the Carreau blood along both the internal inner and outer walls of the artery. For example, in ►Figures 30-33 (30 degrees curvature), the initially blue (low WSS) stenotic zone morphs into a green/yellow zone as the stenotic depth increases and then culminates in a red high WSS zone for 60% stenotic depth. However, with further increment to 80% stenotic depth this red high WSS zone contracts. The relationship is therefore complex. The diastole case always exhibits higher WSS at any stenotic depth. For the 60 degrees curvature case, ►Figures 34-37 show that while the low WSS patterns arise at low stenotic depth (20%), with a small higher WSS zone at the entry, when stenotic depth is increased to 40%, a higher WSS develops along the pre-stenotic zone with maximum WSS again at the entry point and progressive decay in WSS towards the stenotic zone, with low WSS computed again after the stenotic throat (blue zone). The extent of this higher WSS zone is much smaller for the systole case relative to the diastole case. At 60 degrees stenosis, a higher WSS zone emerges at the stenotic throat (green/yellow) for the systole case with a thin boundary layer growing at the inner surface of the outer arterial wall for some distance in the post-stenotic zone. However, for the diastole case, much greater WSS magnitudes are computed at the stenotic zone (red/orange contours) and the growth of the post stenotic near-wall zone is much greater extending almost to the end of the post-stenotic region. This complex variation in WSS is also related to the velocity distribution and influenced by the shear-thinning nature of the Carreau rheological blood. At maximum stenosis depth, the stenotic and post-stenotic acceleration zones are both diminished although a high WSS is sustained at the central stenotic zone in the latter. Low WSS generally dominate the pre- and post-stenotic regimes at this maximum stenotic depth (blue contour zones). These effects are further amplified as the degree of curvature is increased to 90 degrees ►Figures 38-41. The downstream outer wall experiences higher WSS. WSS contours also spread at the outer bend of the arterial wall near the throat and downstream, which is associated with promoting further development of plaque (deposits on the inner walls associated with the greater

stenotic depths). This also increases the risk of atherosclerosis plaque rupture. Again, the maximum acceleration zone in the 90-degree curvature case arises with 60 % stenosis, not the maximum stenotic depth (80%). The final computations for the CFD analysis are the velocity vector plots which permit a clearer visualization of the direction of the Carreau blood flow as depicted in ►Figures 42-53. The results indicate the existence of flow re-circulation downstream of the stenosis. The recirculation is evident at the 40% stenosis and the recirculation zones is substantially amplified for all three curvature cases (30, 60, 90 degrees) as the stenosis depth is increased. This is due to the artery expansion caused by the pulsatile flow. This flow after the stenosis has laminar characters with clear reversed flow in the vicinity of the arterial wall. The most significant accentuation in re-circulation of the Carreau blood flow in the post-stenotic zone is associated with the 60% and 80% stenoses for the 90-degree curvature case ►Figures 52, 53. Again, the vector plots indicate significant deviation in non-Newtonian blood flow relative to conventional Newtonian blood flow, as evident in previous Newtonian studies [6-8].

The structural (stress) analysis computations are shown in ►Figures 54-77 for the FSI analysis. These contour plots are strongly dependent on the elasticity of the artery wall. The Von Mises stress ►Figures 54-65 is highly dependent on the thickness and the curvature of the artery. As mentioned above; to maintain the flow rate, the upstream artery walls experience high stresses which cause contraction in the arteries. The stress is generally higher with larger stenosis. The downstream arterial wall generally experiences low Von Mises stress (blue zones) for all curvatures and stenosis depths. Clearly a significant modification does arise due to the hemodynamic influence on the arterial stress states (one-way coupling). Peak Von Mises stress is always located in the pre-stenotic zone and maximized at the throat stenosis with progressive reduction in the post-stenotic zone. Finally, ►Figures 66-77 display the deformation (total displacement) contours which exhibit a similar trend with the change in stenosis, to the Von Mises elastic stresses. As the stenosis increases, the deformation affects the throat area until it reaches 80% stenosis, where the inlet outer wall of curvature is most severely affected. This indicates a greater potential for rupture of the artery. At higher (90 degrees) curvature, the localization of high displacement in the stenotic region also tends to spread to other locations on the arterial wall, however the high displacement zones are generally sustained for some distance downstream of the stenosis also.

5. Conclusions

Detailed CFD and FSI simulations of non-Newtonian hemodynamics in a curved arterial section with differ-

ent stenosis depths have been described. ANSYS FLUENT has been deployed for the CFD computations with one-way FSI utilized in ANSYS workbench for stress analysis of the arterial walls. Extensive visualization of blood flow patterns relevant to patient-specific conditions is included using both the non-Newtonian (Carreau shear-thinning) bio-rheological model for 30, 60 and 90-degree curvatures, and 20, 40, 60 and 80% stenotic depths. Velocity, pressure, wall shear stress (WSS), Von Mises stress and strain characteristics are all computed for these curvature and stenotic depth scenarios. The results presented accurately predicted the characteristics contributing to cardiovascular diseases in rheological blood flow. The main conclusions of the simulations can be summarized as follows:

(i) The Von Mises stress is substantially influenced by the thickness and the curvature of the artery and is generally higher with larger stenosis. The downstream arterial wall generally experiences low Von Mises stress (blue zones) for all curvatures and stenosis depths. Clearly a significant modification does arise due to the hemodynamic influence on the arterial stress states (one-way coupling). Peak Von Mises stress is always located in the pre-stenotic zone and maximized at the throat stenosis with progressive reduction in the post-stenotic zone.

(ii) Wall deformation (total displacement) contours show similar patterns with the change in stenosis, to the Von Mises elastic stresses. As the stenosis increases, the deformation affects the throat area until the most severe case of 80% stenosis, where the inlet outer wall of curvature is most severely affected. This indicates a greater potential for rupture of the artery.

(iii) Hemodynamic velocity is substantially greater in the diastole compared to the systole for all cases, owing to the compression in the artery by the contraction of the myocardium during systole. Principal blood flow occurs during diastole, increasing the blood flow. The maximum velocity is computed at the throat area (stenosis) and slowly reduces as it reaches the outlet. The velocity magnitude increases as the percentage of stenosis increases; however larger high velocity zones are computed for the 40% case (red area) relative to other stenosis depths. The variation in the post-stenotic region is quite apparent and is exacerbated with greater curvature (60 and 90 degrees) and larger stenosis depths.

(iv) Low wall shear stress arises at the entry zone (pre-stenotic) and again in the exit zone (post-stenotic), although initially for the 30 degrees curvature at low stenosis there is a higher wall shear stress immediately at the entry. However, the high WSS is identified generally along the stenosis throat zone indicating that flow acceleration here produces faster shearing in the Carreau blood along both the internal inner and outer walls of the artery. At 60 degrees stenosis, a higher WSS zone emerges at the stenotic throat (green/yellow) for the

systole case with a thin boundary layer growing at the inner surface of the outer arterial wall for some distance in the post-stenotic zone. However, for the diastole case, much greater WSS magnitudes are computed at the stenotic zone (red/orange contours) and the growth of the post stenotic near-wall zone is much greater extending almost to the end of the post-stenotic region. This complex variation in WSS is also related to the velocity distribution and influenced by the shear-thinning nature of the Carreau rheological blood. At maximum stenosis depth, the stenotic and post-stenotic acceleration zones are both diminished although a high WSS is sustained at the central stenotic zone in the latter. These effects are further amplified as the degree of curvature is increased to 90 degrees. WSS contours also spread at the outer bend of the arterial wall near the throat and downstream, which is associated with promoting further development of plaque (deposits on the inner walls associated with the greater stenotic depths).

(v) For all three curvature cases (with 4 stenotic depths per case) the pressure in the Carreau blood flow is generally much higher upstream of the stenosis when compared to the downstream. The local pressure drop after the flow passes through stenosis is attributable to the constriction which induces acceleration but by virtue of Bernoulli's equation, manifests in a pressure slump. The pressure drops further with the flow rate increase, the pressure difference is elevated as the stenosis is increased, which is associated with clinical diseases and plaque deposition.

Overall, using CFD and FSI, the risk of plaque formation can be predicted, and the computations described provide an understanding of the parameters which are most influential in predicting plaque formation and plaque rupture. The wall shear stress obtained from CFD simulations can be used to predict such phenomena; however, FSI provides the most accurate picture of how the artery reacts to the formation of stenosis with different curvature. Of course, as in all simulations, there are some assumptions involved in the analysis which restrict the full understanding of the study. Since the blood flow behaves in a pulsatile manner, an unsteady FSI analysis is required which can be explored in future investigations. Furthermore, more detailed visualization of the dual Dean vortex structure may be addressed with more refined mesh densities and also the effect of oscillatory parameters (e.g. Womersley number) can be examined to determine the frequency and phase of the flow. Additionally, pressure gradients may also be of a decaying nature which contribute to

the continuous decrease of velocity in a blood flow. Finally other non-Newtonian models may be deployed for the hemo-rheology e. g. Casson and viscoelastic user defined models. All these aspects are under consideration and efforts in these directions are underway and will be reported imminently.

Acknowledgements

The authors are grateful to both reviewers for their comments which have improved the clarity of the present article.

Research ethics

Not applicable.

Author contributions

Conceptualization: [S. Kuharat, M. A. Chaudhary], Methodology: [All 4 authors], Formal Analysis: [M. A. Chaudhary], Investigation: [All 4 authors], Resources: [SKuharat and M. A. Chaudhary], Data Curation: [M. A. Chaudhary], Writing - Original Draft Preparation: [All 4 authors], Writing - Review & Editing: [All A authors], Visualization: [M. A. Chaudhary], Supervision: [S. Kuharat and O. A. Beg], Project Administration: [S. Kuharat]

Competing interests

The author(s) declare(s) no conflict of interest.

Research funding

None declared.

Data availability


Not applicable.

Peer-review

Externally peer-reviewed.

Orcid

Sireetorn Kuharat  <https://orcid.org/0009-0000-5739-9137>

M. A. Chaudhry  <https://orcid.org/0000-0001-7611-9356>

O. Anwar Bég  <https://orcid.org/0000-0001-5925-6711>

Tasveer A. Bég  <https://orcid.org/0009-0004-1023-8255>

References

- [1] Papageorgiou, N. (2016). *Cardiovascular diseases: Genetic susceptibility, environmental factors and their interaction*. Academic Press.
- [2] Goldsmith, H. L., & Skalak, R. (1975). Hemodynamics. *Annual Review of Fluid Mechanics*, 7(1), 213-247.
- [3] Ku, D. N. (1997). Blood flow in arteries. *Annual Review of Fluid Mechanics*, 29(1), 399-434.
- [4] Taylor, C. A., & Figueroa, C. A. (2009). Patient-specific modelling of cardiovascular mechanics. *Annual Review of Biomedical Engineering*,

- 11, 109-134.
- [5] Wong, K. K., Wu, J., Liu, G., Huang, W., & Ghista, D. N. (2020). Coronary arteries hemodynamics: Effect of arterial geometry on hemodynamic parameters causing atherosclerosis. *Medical & Biological Engineering & Computing*, 58, 1831-1843.
- [6] Berger, S. A., & Jou, L.-D. (2000). Flows in stenotic vessels. *Annual Review of Fluid Mechanics*, 32, 347-382.
- [7] Dash, R. K., Jayaraman, G., & Mehta, K. N. (1999). Flow in a catheterized curved artery with stenosis. *Journal of Biomechanics*, 32(1), 49-61.
- [8] Kim, J., Jin, D., Choi, H., Kweon, J., Yang, D. H., & Kim, Y. H. (2020). A zero-dimensional predictive model for the pressure drop in the stenotic coronary artery based on its geometric characteristics. *Journal of Biomechanics*, 113, 110076.
- [9] Santamarina, A., Weydahl, E., Siegel, J. M., & Moore, J. E. (1998). Computational analysis of flow in a curved tube model of the coronary arteries: Effects of time-varying curvature. *Annals of Biomedical Engineering*, 26, 944-954.
- [10] Hoque, M. M., Alam, M. M., & Ferdows, M. (2013). Numerical simulation of Dean number and curvature effects on magneto-biofluid flow through a curved conduit. *Proceedings of the Institution of Mechanical Engineers, Part H: Journal of Engineering in Medicine*, 227(11), 1155-1170.
- [11] Chiang, C. H., Kao, R. H., Hung, T. K., & Bég, O. A. (2023). Computation of three-dimensional blood flow development in a 180° curved tube geometry. *Journal of Mechanics in Medicine and Biology*.
- [12] Ali, N., Javid, K., Sajid, M., & Bég, O. A. (2016). Numerical simulation of peristaltic flow of a biorheological fluid with shear-dependent viscosity in a curved channel. *Computer Methods In Biomechanics and Biomedical Engineering*, 19(6), 614-627.
- [13] Tripathi, D., Akbar, N. S., Khan, Z. H., & Bég, O. A. (2016). Peristaltic transport of bi-viscosity fluids through a curved tube: A mathematical model for intestinal flow. *Proceedings of the Institution of Mechanical Engineers, Part H: Journal of Engineering in Medicine*, 230(9), 817-828.
- [14] Narla, V. K., Tripathi, D., & Bég, O. A. (2020). Electro-osmotic nanofluid flow in a curved microchannel. *Chinese Journal of Physics*, 67, 544-558.
- [15] Khan, A. A., Akram, K., Zaman, A., & Bég, T. A. (2022). Electro-osmotic peristaltic flow and heat transfer in an ionic viscoelastic fluid through a curved micro-channel with viscous dissipation. *Proceedings of the Institution of Mechanical Engineers, Part H: Journal of Engineering in Medicine*, 236(8), 1080-1092.
- [16] Bég, O. A., Hoque, M. M., Wahiduzzaman, M., Alam, M. M., & Ferdows, M. (2014). Spectral numerical simulation of magneto-physiological laminar dean flow. *Journal of Mechanics in Medicine and Biology*, 14(04), 1450047.
- [17] Zaman, A., Ali, N., & Bég, O. A. (2016). Unsteady magnetohydrodynamic blood flow in a porous-saturated overlapping stenotic artery—Numerical modelling. *Journal of Mechanics in Medicine and Biology*, 16(04), 1650049.
- [18] Wajihah, S. A., & Sankar, D. S. (2023). A review on non-Newtonian fluid models for multi-layered blood rheology in constricted arteries. *Archive of Applied Mechanics*, 93(5), 1771-1796.
- [19] Sriyab, S. (2020). The effect of stenotic geometry and non-Newtonian property of blood flow through arterial stenosis. *Cardiovascular & Haematological Disorders-Drug Targets*, 20(1), 16-30.
- [20] Lakzian, E., & Akbarzadeh, P. (2019). Numerical investigation of unsteady pulsatile Newtonian/non-Newtonian blood flow through curved stenosed arteries. *Bio-Medical Materials and Engineering*, 30(5-6), 525-540.
- [21] Zaman, A., Ali, N., Anwar Bég, O., & Bég, T. A. (2016). Numerical simulation of unsteady micropolar hemodynamics in a tapered catheterized artery with a combination of stenosis and aneurysm. *Medical & Biological Engineering & Computing*, 54, 1423-1436.
- [22] Vasu, B., Dubey, A., Bég, O. A., & Gorla, R. S. (2020). Micropolar pulsatile blood flow conveying nanoparticles in a stenotic tapered artery: Non-Newtonian pharmacodynamic simulation. *Computers in Biology and Medicine*, 126, 104025.
- [23] Tripathi, J., Vasu, B., Bég, O. A., & Gorla, R. S. R. (2021). Unsteady hybrid nanoparticle-mediated magneto-hemodynamics and heat transfer through an overlapped stenotic artery: Biomedical drug delivery simulation. *Proceedings of the Institution of Mechanical Engineers, Part H: Journal of Engineering in Medicine*, 235(10), 1175-1196.
- [24] Dubey, A., Vasu, B., Bég, O. A., & Gorla, R. S. R. (2020). Computational fluid dynamic simulation of two-fluid non-Newtonian nanohemodynamics through a diseased artery with a stenosis and aneurysm. *Computer Methods in Biomechanics and Biomedical Engineering*, 23(8), 345-371.
- [25] Tripathi, J., Vasu, B., & Bég, O. A. (2021). Computational simulations of hybrid mediated nano-hemodynamics (Ag-Au/Blood) through an irregular symmetric stenosis. *Computers in Biology and Medicine*, 130, 104213.
- [26] Roy, A. K., & Bég, O. A. (2021). Asymptotic study of unsteady mass transfer through a rigid artery with multiple irregular stenoses. *Applied Mathematics and Computation*, 410, 126485.
- [27] Zaman, A., Ali, N., Bég, O. A., & Sajid, M. (2016). Heat and mass transfer to blood flowing through a tapered overlapping stenosed artery. *International Journal of Heat and Mass Transfer*, 95, 1084-1095.
- [28] Zaman, A., Ali, N., Bég, O. A., & Sajid, M. (2016). Unsteady two-layered blood flow through an a-shaped stenosed artery using the generalized Oldroyd-B fluid model. *The ANZIAM Journal*, 58(1), 96-118.
- [29] Akbar, N. S., Tripathi, D., & Bég, O. A. (2017). Variable-viscosity thermal hemodynamic slip flow conveying nanoparticles through a permeable-walled composite stenosed artery. *The European Physical Journal Plus*, 132, 1-11.
- [30] Ali, N., Zaman, A., Sajid, M., Bég, O. A., Shamshuddin, M. D., & Kadir, A. (2018). Numerical simulation of time-dependent non-Newtonian nano-pharmacodynamic transport phenomena in a tapered overlapping stenosed artery. *Nanoscience and Technology: An International Journal*, 9(3).
- [31] Bukač, M., Čanić, S., Tambača, J., & Wang, Y. (2019). Fluid–structure interaction between pulsatile blood flow and a curved stented coronary artery on a beating heart: A four stent computational study. *Computer Methods in Applied Mechanics and Engineering*, 350, 679-700.
- [32] Bukač, M., Čanić, S., Glowinski, R., Tambača, J., & Quaini, A. (2013). Fluid–structure interaction in blood flow capturing non-zero longitudinal structure displacement. *Journal of Computational Physics*, 235, 515-541.
- [33] Mendez, V., Di Giuseppe, M., & Pasta, S. (2018). Comparison of hemodynamic and structural indices of ascending thoracic aortic aneurysm as predicted by 2-way FSI, CFD rigid wall simulation and patient-specific displacement-based FEA. *Computers in Biology and Medicine*, 100, 221-229.
- [34] Carvalho, V., Lopes, D., Silva, J., Puga, H., Lima, R. A., Teixeira, J. C., & Teixeira, S. (2022). Comparison of CFD and FSI simulations of blood flow in stenotic coronary arteries. In S. Bhattacharyya (Ed.), *Applications of Computational Fluid Dynamics Simulation and Modeling*. Intech Open Publishers.
- [35] Luraghi, G., Wu, W., De Gaetano, F., Matas, J. F. R., Moggridge, G. D., Serrani, M., & Migliavacca, F. (2017). Evaluation of an aortic valve prosthesis: Fluid-structure interaction or structural simulation? *Journal of Biomechanics*, 58, 45-51.
- [36] Failer, L., Minakowski, P., & Richter, T. (2021). On the impact of fluid structure interaction in blood flow simulations: Stenotic coronary artery benchmark. *Vietnam Journal of Mathematics*, 49, 169-187.
- [37] Balzani, D., Heinlein, A., Klawonn, A., Rheinbach, O., & Schröder, J. (2023). Comparison of arterial wall models in fluid–structure interaction simulations. *Computational Mechanics*, 2, 1-7.
- [38] DeParis, S., Forti, D., Heinlein, A., Klawonn, A., Quarteroni, A., & Rheinbach, O. (2015). A comparison of preconditioners for the Steklov–Poincaré formulation of the fluid-structure coupling in hemodynamics. *PAMM*, 15(1), 93-94.
- [39] Gasser, T. C., Miller, C., Polzer, S., & Roy, J. (2023). A quarter of a century biomechanical rupture risk assessment of abdominal aortic aneurysms. Achievements, clinical relevance, and ongoing deve-

- lopments. *International Journal of Numerical Methods in Biomedical Engineering*, 39(4), e3587.
- [40] Turek, S., Hron, J., Madlik, M., Razzaq, M., Wobker, H., & Acker, J. F. (2010). Numerical simulation and benchmarking of a monolithic multigrid solver for fluid-structure interaction problems with application to hemodynamics. In H.-J. Bungartz et al. (Eds.), *Fluid Structure Interaction II*, Lecture Notes in Computational Science and Engineering (Vol. 73). Springer Berlin, Heidelberg.
- [41] Bertaglia, G., Caleffi, V., & Valiani, A. (2020). Modeling blood flow in viscoelastic vessels: The 1D augmented fluid–structure interaction system. *Computer Methods in Applied Mechanics and Engineering*, 360, 112772.
- [42] Charalambos, V., Michael, O., & Wilmer, W. N. (2012). *McDonald's blood flow in arteries: Theoretical, experimental and clinical principles* (6th ed.). CRC Press.
- [43] Mamun, K., Akhter, M., & Ali, M. (2016). Physiological non-Newtonian blood flow through single stenosed artery. *Theoretical and Applied Mechanics*, 43, 99–115.
- [44] Gendy, M. E., Bég, O. A., Kadir, A., Islam, M. N., & Tripathi, D. (2021). Computational fluid dynamics simulation and visualization of Newtonian and non-Newtonian transport in a peristaltic micro-pump. *Journal of Mechanics in Medicine and Biology*, 21(08), 2150058.
- [45] Ali, N., Asghar, Z., Sajid, M., & Bég, O. A. (2020). Biological interactions between Carreau fluid and micro-swimmers in a complex wavy canal with MHD effects. *Journal of the Brazilian Society of Mechanical Sciences and Engineering*, 41, 446.
- [46] Dubey, A., Vasu, B., Bég, O. A., & Gorla, R. S. R. (2021). Finite element computation of magneto-hemodynamic flow and heat transfer in a bifurcated artery with saccular aneurysm using the Carreau-Yasuda biorheological model. *Microvascular Research*, 138, 104221.
- [47] Muhammed, R. K., Basha, H., Reddy, G. J., Shankar, U., & Bég, O. A. (2022). Influence of variable thermal conductivity and dissipation on magnetic Carreau fluid flow along a micro-cantilever sensor in a squeezing regime. *Waves in Random and Complex Media*, 1–30.
- [48] Gambaruto, A., Janela, J., Moura, A., & Sequeira, A. (2013). Shear-thinning effects of hemodynamics in patient-specific cerebral aneurysms. *Mathematical Biosciences and Engineering*, 10, 649–667.
- [49] Frolov, S. V., Sindeev, S. V., Liepsch, D., & Balasso, A. (2016). Experimental and CFD flow studies in an intracranial aneurysm model with Newtonian and non-Newtonian fluids. *Technology and Health Care*, 24, 317–333.
- [50] Gijsen, F. J. H., van de Vosse, F. N., & Janssen, J. D. (1999). The influence of the non-Newtonian properties of blood on the flow in large arteries: Steady flow in a carotid bifurcation model. *Journal of Biomechanics*, 32, 601–608.
- [51] ANSYS. (2021). *ANSYS FLUENT Theory Manual* (Version 21). Lebanon, NH: ANSYS, Inc.
- [52] Ghigo, A. R., Wang, X. F., Armentano, R., Fullana, J. M., & Lagrée, P. Y. (2017). Linear and nonlinear viscoelastic arterial wall models: Application on animals. *Journal of Biomechanical Engineering*, 139(1), 011003.